

HIGH-GRADIENT NANOMAGNET-ON-CANTILEVER
FABRICATION FOR SCANNED PROBE DETECTION OF
MAGNETIC RESONANCE

A Dissertation

Presented to the Faculty of the Graduate School

of Cornell University

in Partial Fulfillment of the Requirements for the Degree of

Doctor of Philosophy

by

Jonilyn Greta Longenecker

January 2013

© 2013 Jonilyn Greta Longenecker

ALL RIGHTS RESERVED

HIGH-GRADIENT NANOMAGNET-ON-CANTILEVER FABRICATION FOR
SCANNED PROBE DETECTION OF MAGNETIC RESONANCE

Jonilyn Greta Longenecker, Ph.D.

Cornell University 2013

Magnetic resonance force microscopy (MRFM) is a non-invasive, three-dimensional imaging technique that employs attonewton-sensitivity cantilevers to mechanically detect the interaction between the field gradient of a magnetic particle and magnetically-active sample spins. Achieving high sensitivity demands the use of a high field gradient. In order to study a wide range of samples, it is equally desirable to locate the magnetic tip on the cantilever.

The work in this thesis centers on the development of nanomagnets on cantilevers that produce sufficiently large field gradients for nanometer-scale nuclear spin MRFM imaging and single electron spin detection. A new fabrication protocol is introduced to prepare nickel and cobalt nanomagnets on cantilevers. Custom attonewton-sensitivity cantilevers were batch fabricated. Nanomagnets were prepared separately on micrometer-scale silicon chips using electron beam lithography and electron beam deposition. Each magnet-tipped silicon chip was serially attached to a cantilever using focused ion beam manipulation. Frequency-shift cantilever magnetometry and superconducting quantum interference device magnetometry were used to assess the nanomagnet magnetization. X-ray photoelectron spectroscopy was used to determine the extent of oxidation damage.

A cobalt nanomagnet-tipped chip attached to an attonewton-sensitivity cantilever was used to detect statistical fluctuations in the proton magnetization of a polystyrene film. MRFM signal was studied versus rf irradiation frequency and tip-sample separation. The tip-field gradient $\partial B_z^{\text{tip}} / \partial z$ of the nanomagnet was estimated to be between 4.4 and 5.4 MT m⁻¹, which is comparable to the gradient used in recent 4 nm resolution ¹H imaging experiments

and nearly an order of magnitude larger than the gradients achieved in prior magnet-on-cantilever MRFM experiments. These magnet-tipped cantilevers are projected to achieve a proton imaging resolution of 5 to 10 nm.

The key design considerations and development of a new magnetic resonance force microscope are also discussed in this thesis. The microscope will use the newly-developed nanomagnet-tipped cantilevers to conduct high-resolution, three-dimensional MRFM imaging experiments at cryogenic temperatures, in high vacuum, and at magnetic fields up to 9 T.

Overall, the work in this thesis has significantly advanced the capabilities of MRFM and has poised the field to begin conducting high-resolution imaging experiments on a broad range of previously-inaccessible samples.

BIOGRAPHICAL SKETCH

Jonilyn Longenecker grew up in Lancaster, Pennsylvania. At an early age, she developed lasting interests in music, mathematics, and science. She gained her first appreciation for conducting scientific research through participation in high school science fair projects on designs for improved passive solar power Trombe walls.

Jonilyn attended Juniata College for her undergraduate education, where she earned a major in chemistry and a minor in mathematics. While taking chemistry courses at Juniata, she became fascinated by chemical characterization and explored a variety of physical chemistry independent research projects. She conducted simulations-based research on the binding affinity of novel drug targets for two summers. After her junior year, she participated in a Research Experience for Undergraduates (REU) program at the University of Hawaii at Manoa and completed an experimental astrochemistry project on the reaction dynamics after irradiation of diboranyl ices. Through this summer REU project and her senior thesis on diffusion NMR, Jonilyn learned that her passion lies in experimental research.

In graduate school at Cornell University, Jonilyn sought to combine her interest in experimental chemistry with interdisciplinary applications. By joining Professor John Marohn's research project on magnetic resonance force microscopy, she gained extensive experience in the nanofabrication of high-compliance force sensors and co-developed a third-generation magnetic resonance force microscope. During her graduate career Jonilyn presented at more than 15 conferences, including invited talks at a NanoMRI Conference in Ascona, Switzerland and at a Gordon Research Conference on Nanostructure Fabrication. She was selected to participate in the 2010 National Nanotechnology Infrastructure Network International Winter School for Graduate Students at the Indian Institute for Science in Bangalore, India. In 2011 she also received a Best Paper Award in the MEMS and NEMS division of the American Vacuum Society International Symposium and the Nellie Yeh-Poh Lin Whetten Memorial Award from the Cornell Center for NanoScale Science and Technology.

To my parents, Dave and Karen Longenecker,
for inspiring, guiding, and encouraging me to always pursue my dreams.

ACKNOWLEDGEMENTS

Thanks first goes to my advisor, John Marohn. Thank you for encouraging me, pushing me, and giving me room to grow into an independent researcher. Your enthusiasm and creativity have been a perpetual source of inspiration. By fostering a group culture that values collaboration, positive outlooks, and an awareness of the scientific community around us, you have given me a home within Cornell in which I could thrive and contribute. Thanks and gratitude also goes to my committee members, David Muller, Jiwoong Park, and Poul Petersen, for their guidance during my graduate career.

I have had a wonderful group of coworkers during my time at Cornell. Early on Steve Hickman taught me the ropes of Cornell's cleanroom and the fabrication techniques for integrated magnet-tipped cantilevers. Eric Moore mentored me on conducting magnetic resonance force microscopy (MRFM) experiments and collaborated on frequency-shift cantilever magnetometry experiments. Both Eric Moore and Lei Chen, who helped to co-design the third-generation magnetic resonance force microscope, taught me a great deal about designing, constructing, and testing a cryogenic system. Thanks to Alex Senko for his contributions to the characterization of thin-film magnetic materials. Thanks also to the rest of the Marohn group for being such a fun group of people to work alongside every day. Best of luck to the next generation of MRFM students, Paméla Nasr and Christine Gleave, as you further the development of the microscope and launch the applications-based phase of our team's MRFM studies.

I am also grateful to many others for collaboration and assistance. Thanks to Daniel Rugar and John Mamin at the IBM Almaden Research Center for conducting a joint NMR-MRFM experiment. Through interactions with you I grew as both a scientist and as a scientific writer. Thanks also to collaborators Doran Smith at the Army Research Laboratory and Lee Harrell at West Point Military Academy for sharing their expertise and creativity on the development of a new MRFM probe. Cornell's Research Services Shop and Laboratory

of Atomic and Solid State Physics Machine Shop were invaluable during the construction of the new magnetic resonance force microscope. My nanofabrication work was greatly aided by interactions with the staff at the Cornell NanoScale Science and Technology Facility; thanks specifically goes to Daron Westly, Rob Ilic, Vince Genova, Meredith Metzler, and Alan Bleier. Thanks also to Mick Thomas at the Cornell Center for Materials Research for teaching me how to use the focused ion beam microscope and for always being available to trouble-shoot the tool. Additional collaborators, and the specific contributions that each made to data presented in this thesis, are acknowledged at the end of each thesis chapter.

My family and friends have provided balance, support, and encouragement during my time in graduate school. Thanks to my parents for your unconditional love and support. You have given me an amazing foundation, and have instilled in me both a strong moral center and the gumption to follow through and complete what I pursue. Thanks to my fiancé, Jonathan Yoder, for being an incredible partner and listener. I am looking so forward to starting our life together. Thanks to Chin Subban for all of the awesome restaurant testing adventures, cooking experiments, and shopping excursions. It meant so much that you were always there to celebrate the good times and commiserate when things were stressful. Thanks also to Marie Krysak for all of our relaxing taco and game nights and to Michele Tague for making me laugh more times than I could ever count. Thanks to the first-year physical chemistry homework crew. I learned so much from all of you, and you even greatly improved my skills at ping-pong for a few months! And thanks to all of the friends I have made in the CNF — you made the cleanroom a warm, friendly, and fun place to work.

The work in this thesis was funded by the National Science Foundation through the Cornell Center for Nanoscale Systems (Grant Nos. EEC-0117770 and EEC-0646547), the National Institutes of Health (Grant No. 5R01GM-070012), and the Army Research Office MultiUniversity Research Initiative (Grant No. W911NF-05-1-0403). The research presented in this thesis made use of the facilities at the Cornell Center for Materials Research, which is

supported by the National Science Foundation Materials Research Science and Engineering Centers program (Grant No. DMR-0520404), and the Cornell NanoScale Science and Technology Facility (CNF), a member of the National Nanotechnology Infrastructure Network supported by the National Science Foundation (Grant No. ECS-0335765).

TABLE OF CONTENTS

| | |
|--|-----------|
| Biographical Sketch | iii |
| Dedication | iv |
| Acknowledgements | v |
| Table of Contents | viii |
| List of Figures | xii |
| List of Tables | xiii |
| | |
| 1 Introduction to Magnetic Resonance Force Microscopy | 1 |
| 1.1 The MRFM Experiment | 6 |
| 1.2 Dependence of MRFM Sensitivity on the Magnetic-Field Gradient and Force Fluctuations | 11 |
| 1.2.1 Minimizing Force Fluctuations for Magnet-Tipped Attnewton-Sensitivity MRFM Cantilevers | 12 |
| 1.2.2 Optimizing the Magnetic Field Gradient of Magnet-Tipped MRFM Cantilevers | 14 |
| 1.3 Outline of the Dissertation | 17 |
| | |
| 2 Magnet-on-Cantilever Precedent and Integrated Magnet-on-Cantilever Fabrication | 21 |
| 2.1 Introduction | 21 |
| 2.2 Prior Magnet-on-Cantilever Fabrication Methods and Results | 22 |
| 2.3 Process Integration Challenges of the Overhanging Nanomagnet-on-Cantilever Fabrication Protocol | 26 |
| 2.4 Barrier Layers Introduced to Prevent Nanomagnet Damage | 37 |
| 2.5 Discussion | 43 |
| 2.6 Moving Forward: A New Protocol is Needed to Improve Yield and Magnetization of Magnet-Tipped Cantilevers | 45 |
| | |
| 3 Magnet-Tipped Chip Fabrication and Attachment to Attnewton-Sensitivity Cantilevers by Focused Ion Beam Manipulation | 50 |
| 3.1 Introduction | 50 |
| 3.2 Nickel Nanomagnet-Tipped Chip Fabrication Protocol | 51 |
| 3.3 Summary of Blank Cantilever Fabrication | 55 |
| 3.4 Focused Ion Beam Lift-Out and Attachment to Cantilevers | 58 |
| 3.5 Nanomagnet-Tipped Chip Process Yield | 60 |
| 3.6 Switching to Cobalt Magnets | 64 |
| 3.7 Improvements to the Chip Design | 67 |
| 3.7.1 Side Tabs Added to Magnet-Tipped Chips | 67 |
| 3.7.2 Fabrication of Non-Overhanging Magnet Chips | 71 |
| 3.7.3 Incorporation of Release Chips | 72 |
| 3.8 Chip Release by HF Vapor | 74 |
| 3.9 Discussion | 79 |

| | |
|--|------------|
| 4 Nickel and Cobalt Magnetic Material Characterization | 82 |
| 4.1 Initial Frequency-Shift Cantilever Magnetometry Studies on Nickel Nanomagnets | 82 |
| 4.2 Hypotheses to Explain the Low Magnetization of the Nickel Nanomagnets | 87 |
| 4.3 Nickel and Cobalt Magnetic Material Analysis | 90 |
| 4.3.1 SQUID Magnetometry Sample Preparation | 91 |
| 4.3.2 SQUID Magnetometry Analysis and Results | 93 |
| 4.3.3 XPS Sample Preparation | 97 |
| 4.3.4 XPS with Depth Profiling Analysis and Results | 98 |
| 4.4 Reassessing Frequency-Shift Cantilever Magnetometry: Studying a Cobalt Nanomagnet | 104 |
| 4.5 Discussion | 106 |
| 5 High-Gradient Cobalt Nanomagnets on Cantilevers Used to Sensitive Detect Nuclear Magnetic Resonance | 110 |
| 5.1 Introduction | 110 |
| 5.2 Experimental Methods | 112 |
| 5.2.1 Magnet-Tipped Cantilever Characterization | 112 |
| 5.2.2 Magnetic Material Characterization | 115 |
| 5.2.3 Sample and Microwire Preparation | 116 |
| 5.2.4 Spin Detection Protocol | 116 |
| 5.3 Magnet-on-Cantilever Detection of Nuclear Magnetic Resonance | 118 |
| 5.4 Calculating the Tip-Field Gradient of the Cobalt Nanomagnet | 120 |
| 5.5 Dissipation and Frequency Fluctuations | 123 |
| 5.6 Discussion | 127 |
| 6 Building the Third-Generation Cornell Magnetic Resonance Force Microscope | 131 |
| 6.1 Introduction | 131 |
| 6.2 MRFM Microscope Superstructure | 134 |
| 6.2.1 Vibrational Isolation of the MRFM Microscope | 134 |
| 6.2.2 Narrow-Neck Liquid Helium Dewar | 137 |
| 6.2.3 Dual Hoist System | 140 |
| 6.3 Third-Generation MRFM Probe Body | 142 |
| 6.3.1 Vacuum-Compatible MRFM Probe Body Design | 143 |
| 6.3.2 Vacuum Feedthroughs | 147 |
| 6.3.3 Mitigating Blackbody Radiation | 149 |
| 6.4 Third-Generation MRFM Probe Head | 150 |
| 6.4.1 Probe Head Design | 150 |
| 6.4.2 Heat Sinking of the Probe Head | 151 |
| 6.4.3 Hang-Down Geometry | 153 |
| 6.4.4 Pan-Walker Stage with Three-Dimensional Motion | 155 |
| 6.4.5 Coplanar Waveguides | 158 |
| 6.5 Discussion | 160 |

| | |
|---|------------|
| 7 Overall Conclusions and Outlooks for the Next Generation of Cornell MRFM Fabrication | 163 |
| A Protocol for the Fabrication of Nanomagnet-Tipped Silicon Chips | 169 |
| A.1 Wafer Layout | 170 |
| A.2 Alignment Marks | 173 |
| A.3 Chip Design and Release | 175 |
| A.4 Nickel or Cobalt Nanomagnet Deposition | 178 |
| A.5 Silicon Underetch of U-Shaped Etch Pits | 181 |
| B Focused Ion Beam Process for Lift-Out of Magnet-Tipped Chips and Attachment to Cantilevers | 185 |
| B.1 Loading in Samples and Setting Up for the Magnet-Tipped Chip Release . . | 186 |
| B.2 Releasing the Magnet-Tipped Chip from the Substrate | 188 |
| B.3 Adhering the Magnet-Tipped Chip to a Blank Cantilever and Removing the Probe Needle | 190 |
| B.4 Unloading the Completed Magnet-Tipped Cantilevers | 193 |

LIST OF FIGURES

| | | |
|------|---|----|
| 1.1 | Schematic of a general MRFM experimental setup | 7 |
| 1.2 | Influence of a magnetically-inactive layer on the tip-sample separation for a spherical magnetic particle | 16 |
| 2.1 | Schematics of the key steps of the integrated, overhanging magnet-tipped cantilever fabrication protocol | 29 |
| 2.2 | SEM images of nickel nanomagnets that demonstrate the various forms of magnetic material damage | 30 |
| 2.3 | Magnet-tipped cantilevers processed while coated with a thin residual film | 32 |
| 2.4 | Images of a magnet-tipped cantilever mounted on a TEM grid | 34 |
| 2.5 | STEM image of the overhanging portion of a polycrystalline nickel nanomagnet | 34 |
| 2.6 | EELS spectrum showing the energy loss edges of the elements observed in a nickel nanomagnet | 35 |
| 2.7 | EELS linescans along the leading and side edges of a nickel nanomagnet . . | 36 |
| 2.8 | EELS linescan of an annealed nickel film protected by tantalum and alumina barrier layers | 40 |
| 2.9 | Schematic detailing the incorporation of tantalum and alumina barrier layers . | 41 |
| 2.10 | SEM images of released magnet-tipped cantilevers fabricated using barrier layers | 42 |
| 2.11 | Frequency-shift cantilever magnetometry signal for a nickel nanomagnet fabricated using barrier layers | 43 |
| 3.1 | Damaged e-beam lithography alignment marks | 53 |
| 3.2 | Magnet-tipped chip process flow | 54 |
| 3.3 | Overhanging nickel nanomagnets on magnet-tipped chips | 56 |
| 3.4 | Cantilever handle die and cantilever dimensions | 59 |
| 3.5 | Original FIB lift-out process | 61 |
| 3.6 | Alternative designs for magnet-tipped chip support tethers | 63 |
| 3.7 | Cobalt overhanging nanomagnets on magnet-tipped chips | 65 |
| 3.8 | Revised FIB lift-out procedure | 69 |
| 3.9 | Third-generation magnet-tipped chip design | 71 |
| 3.10 | Non-overhanging magnet chips | 72 |
| 3.11 | Release chips | 73 |
| 3.12 | HF vapor release of a nickel magnet-tipped chip | 75 |
| 3.13 | Cobalt nanomagnets damaged by exposure to HF vapor | 77 |
| 3.14 | Influence of substrate roughness on the surface roughness of nanomagnets . | 80 |
| 4.1 | Frequency-shift cantilever magnetometry signal for a nickel nanomagnet . . | 85 |
| 4.2 | Angled views of bent and straight attonewton-sensitivity cantilevers | 89 |
| 4.3 | Frequency-shift cantilever magnetometry simulations to assess the effect of cantilever bending | 89 |
| 4.4 | Illustrations of reduced-magnetization damage scenarios | 90 |
| 4.5 | Ferrometric contamination of SQUID magnetization loops from metal tweezers | 92 |

| | | |
|------|--|-----|
| 4.6 | SQUID in-plane magnetization loops for platinum-capped and uncapped nickel films | 94 |
| 4.7 | SQUID magnetometry analysis of chromium and titanium adhesion layers | 95 |
| 4.8 | SQUID in-plane magnetization loops for platinum-capped and uncapped cobalt films | 96 |
| 4.9 | Assessment of the conversion from XPS etch rate to depth | 100 |
| 4.10 | XPS depth profile of an uncapped nickel film | 101 |
| 4.11 | XPS depth profile of a platinum-capped nickel film | 101 |
| 4.12 | XPS depth profiles of unbaked and baked uncapped cobalt films | 102 |
| 4.13 | XPS depth profiles of unbaked and baked platinum-capped cobalt films | 103 |
| 4.14 | Frequency-shift cantilever magnetometry signal for a cobalt nanomagnet | 105 |
| 5.1 | Schematic of the NMR-MRFM experiment | 112 |
| 5.2 | SEM images of the cobalt magnet-tipped cantilever | 114 |
| 5.3 | MRFM signal for protons in a 40 nm thick polystyrene film | 119 |
| 5.4 | Tip fields and tip-field gradients for the cobalt nanomagnet | 121 |
| 5.5 | Cantilever dissipation and spectral density of force fluctuations versus tip-sample separation | 125 |
| 5.6 | Power spectral density of frequency fluctuations versus modulation frequency . | 126 |
| 6.1 | MRFM microscope superstructure | 132 |
| 6.2 | Vibrational measurements | 136 |
| 6.3 | Bottom-loading liquid helium dewar | 139 |
| 6.4 | Hoist system for the MRFM probe | 141 |
| 6.5 | Third-generation MRFM probe body | 145 |
| 6.6 | Schematics of the assembly to dismantle the vacuum can | 146 |
| 6.7 | Schematics detailing the split ferrule used to feed a coaxial cable from liquid helium into vacuum | 148 |
| 6.8 | Images of the third-generation MRFM probe head | 152 |
| 6.9 | Schematics of the hang-down and SPAM MRFM geometries. | 154 |
| 6.10 | Magnetic damping of a 4 μm nickel magnet attached to an attonewton-sensitivity cantilever | 155 |
| 6.11 | Cartoon showing the stepping mechanism of the Pan-style nanopositioner . | 157 |
| A.1 | Magnet-tipped chip example wafer layout | 172 |

LIST OF TABLES

| | | |
|-----|---|-----|
| 4.1 | Frequency-shift cantilever magnetometry analysis of nickel nanomagnets | 86 |
| 5.1 | Magnetic field gradients achieved in high sensitivity magnetic resonance force microscope experiments | 124 |
| A.1 | Positions of the e-beam lithography alignment marks for the magnet-tipped chip fabrication layers. | 171 |

CHAPTER 1

INTRODUCTION TO MAGNETIC RESONANCE FORCE MICROSCOPY

Three-dimensional imaging techniques have continually revolutionized our understanding of the macroscopic and microscopic world around us. Magnetic resonance imaging, developed in the 1970's, has become a tool routinely used in medicine to non-invasively obtain full three-dimensional maps of soft tissue in the body at millimeter resolution. Techniques such as inductively detected nuclear magnetic resonance (NMR) and X-ray diffraction have been used to determine the atomic-resolution structures of thousands of proteins [1]. However, both NMR and X-ray diffraction require large quantities of purified sample; in addition, X-ray diffraction requires sample crystallization. Optical microscopy has recently become a serious contender in single molecule localization through the development of super-resolution imaging techniques [2–4]. Stochastic optical reconstruction microscopy (STORM) has achieved three-dimensional localization of photoswitchable dyes attached to proteins with 30 nm lateral resolution and 50 nm resolution in the axial dimension when imaging live cells at room temperature [5]. However, further advances will be needed before three-dimensional STORM can be used for structural determination of biological samples, including improving the resolution to better than 5 nm.

Cryogenic electron microscopy is a state-of-the-art method for determining the three-dimensional structure of non-crystalline biological macromolecules. Single particle cryoelectron microscopy (cryo-EM), in which many thousands of identical copies of the molecule of interest are imaged and averaged, often has achieved 2 nm resolution when applied to disordered asymmetric complexes and has reached nearly atomic resolution if stringent symmetry requirements when imaging highly symmetric samples, such as viruses [6]. Electron cryotomography (cryo-ET) is used to study single copies of biomacromolecules and can obtain three-dimensional images by rotating the sample stage between approximately $\pm 70^\circ$. Al-

though the resolution of cryo-ET is slightly lower at 3–8 nm, the key benefit is that cryo-ET can be used to study a single copy of a molecule. Single copy analysis is essential when studying asymmetrical viruses and pleomorphic macromolecular assemblies that have variability in their size and shape [7, 8]. Single copies of biological samples have also been studied by cryo-ET to image the components of neuronal processes [9] and to assess single macromolecules in their native cellular context, which, for example, has enhanced the understanding of disease transmission by imaging the structures of viruses during the process of infection [10] and studying the organization of intact bacterial cells [11].

Magnetic resonance force microscopy (MRFM) is emerging as a cryogenic nanoscale imaging technique that could quickly become complementary to cryogenic electron microscopy. For three-dimensional reconstruction, the 4 to 10 nm resolution achieved by Degen *et al.* [12] in their NMR-MRFM [13–18] experiment is already competitive with the resolution achieved by cryo-ET when applied to single copies of biomacromolecules [19–22] and approaches the resolution often achieved by cryo-EM. MRFM is being developed to study systems that are similar to those analyzed by cryo-EM and cryo-ET, but MRFM has the distinct advantages of using isotopic labeling as a contrast agent and being able to work with many-micrometer thick samples, as long as the features of interest are located near or at the surface. Additionally, MRFM could play an important role in the determination of structures that are challenging to study by cryo-EM. Exosomes are a critical component in cell trafficking, but have rarely been studied by cryo-EM [23]. Proteins smaller than 100–200 kDa, such as membrane proteins, are also difficult to study by cryo-EM since the weak signals from these samples lead to poor contrast with embedded vitrified water and difficulties with orientation determination [7, 21, 24]. Unlike cryoelectron microscopy, which has firm resolution limits set by radiation damage, MRFM is a non-invasive technique with resolution continuing to be enhanced through improvements in sensitivity. With a modest factor of two enhancement in MRFM resolution compared to the experiment in Ref. 12, structural studies of the nuclear

spins in many exciting biomacromolecules and macromolecular complexes will be possible using NMR-MRFM.

In addition to using NMR-MRFM to determine biological structures by imaging their proton spin density, MRFM could also be used to detect and image unpaired electron spin labels on proteins. Imaging of individual electron spins has been demonstrated for E' centers in gamma-irradiated quartz [25]; however, the detection protocol used in the experiment required 13 hours of averaging per point and a sample with an extraordinarily long spin-lattice relaxation time. Although E' centers cannot be incorporated into biological samples, electron spin resonance (ESR) active nitroxide spin labels are commonly used to label cysteine residues in proteins. In conventional pulsed ESR, the tertiary structures of proteins have been determined by measuring the distances between pairs of the nitroxide-labeled residues [26–29]. Since the nitroxide free radical in tempamine (4-amino-2,2,6,6-tetramethyl-1-piperidinyloxy) has a spin-lattice relaxation time that is significantly shorter than what could be detected using the detection protocol of Ref. 25, a new MRFM protocol was developed to enable ESR-MRFM studies of biological samples labeled with tempamine spin probes [30]. The spin detection protocol of Ref. 30 can detect electrons with spin-lattice relaxation times consistent with those observed in tempamine-labeled biological samples ($T_1 > 0.2$ ms at a temperature $T=4.2$ K and external magnetic field $B^{\text{ext}}=0.6$ T) and has been used to detect ESR signal from a tempamine film with a sensitivity of 400 polarized electron spins. The next step will be to improve the sensitivity to detect, and subsequently image, single nitroxide spin labels.

With single-spin imaging capabilities, the key advantage of ESR-MRFM over conventional ESR is that significantly less sample preparation — and less total quantity of sample — would be required. In contrast with conventional ESR measurements, which are limited to the detection of pairwise coupling of nitroxide labels and thus require extensive

sample preparation with site-directed spin labels, ESR-MRFM with single-spin resolution could map the absolute positions of nitroxide labels that are uniformly tagged on just a single copy of the biomacromolecule. For a protein with even just five cysteine residues, 10 separate samples (each with a separate pair of nitroxide labels) would need to be prepared for conventional ESR, whereas only a single sample would be needed for ESR-MRFM. In addition to determining the tertiary structure of proteins, ESR-MRFM could be used, for example, to determine the mode of binding of a DNA- or RNA-protein complex by attaching nitroxide spin labels to either the nucleic acids [31–33] or the binding protein [34].

ESR-MRFM imaging could also contribute to the analysis of organic materials. For instance, it would be an exciting advance to use MRFM to obtain three-dimensional images of the phase morphology in bulk heterojunction (BHJ) solar cells [35], which are comprised of a blend of two semiconducting organic materials. In BHJ solar cells, the lateral morphology has been well-characterized using electron tomography, X-ray diffraction, and scanned probe techniques such as atomic force microscopy and electric force microscopy [36–41]; however, the vertical segregation has rarely been imaged at nanoscale resolution [42] and the three-dimensional morphology is still a field of active debate [43]. ESR-MRFM could be used to assess the full three-dimensional phase morphology at a resolution of a few nanometers by adding tempamine spin probes to either the electron-donor or electron-acceptor polymers that make up the photoactive layer. Since MRFM is non-invasive, a top metal electrode and electrical leads could be attached to enable imaging of sandwich-geometry solar cell devices during operation at cryogenic temperatures. Additionally, MRFM is expected to enable the quantification of the internal electric fields in halogen-containing organic electronic materials and the assessment of charge redistribution when light is applied to the solar cell [44–47].

To realize these exciting imaging applications, a key change to the experimental geometry previously used for high-resolution MRFM imaging [12] is required. MRFM is a scanned-

probe technique conducted at cryogenic temperatures that detects the spin density of a sample as a force or force gradient exerted on a high-compliance cantilever. The force is generated by the interaction between the net magnetic moment of the sample spins and the magnetic field gradient generated by a small ferromagnet. Either the sample or magnet is located on the cantilever, and the other is rigidly fixed in close proximity (see Section 1.1 and Figure 1.1). In the highest-resolution MRFM imaging experiment to date [12], a magnetic tip with a field gradient of 4.2 MT m^{-1} was achieved by fabricating a 200 nm diameter $\text{Fe}_{70}\text{Co}_{30}$ pillar on a flat surface.¹ The resultant high-resolution imaging experiments were conducted after individual copies of tobacco mosaic virus particles were adhered to the leading edge of a high-compliance silicon cantilever. The particles were prepared on the cantilever by dipping the cantilever leading edge in a dilute solution containing the virus and air-drying the sample.

The advance of Ref. 12 has not been extended to the study of more general samples, including the experiments proposed in this section, because few samples are robust enough to be prepared in the manner used by Degen *et al.* Frustratingly, the “sample-on-cantilever” nature of the experiment in Ref. 12 precludes the use of sample cryopreservation techniques widely used in electron microscopy [19–21, 49, 50]. The high-compliance cantilevers used in MRFM experiments also cannot support large samples, such as whole cells or organic semiconductor devices. Efforts have been made to switch to the “magnet-on-cantilever” geometry [25, 30, 51–57], in which the magnetic particle would be attached to the cantilever so that the sample could be prepared on a flat substrate. By moving the sample preparation off of the cantilever, standard preservation techniques used in cryoelectron microscopy could be implemented and the size of the sample would not be limited. However, the highest tip-field gradients produced using previous magnet-tipped cantilever fabrication protocols [25, 53, 54, 56, 57] were almost an order of magnitude lower than the gradient achieved in

¹Here the revised gradient estimate reported in Ref. 48 is used.

Ref. 12 and were unsuitable for high-resolution imaging experiments.

The central challenge taken on in this thesis was the fabrication of ferromagnetic particles on cantilevers with sufficiently large magnetic field gradients to achieve the sensitivity needed for sub-5 nm resolution MRFM imaging of a broad range of samples. In the following sections of this chapter, details of the MRFM experimental setup, basics of the physics governing magnetic resonance, and factors that influence MRFM sensitivity are discussed. This chapter concludes with an outline of the key advances reported in the subsequent chapters of the thesis.

1.1 The MRFM Experiment

MRFM was first proposed by John Sidles in 1991 [13]. Since that time, extensive research has been conducted in the field, which has led to improvements in theory, experimental design, and sensitivity. The basic experimental setup and the physics making MRFM possible are described in this section for the magnet-on-cantilever geometry [16–18]. Although the spin physics is identical for the magnet-on-cantilever and sample-on-cantilever (also known as magnet-on-surface) geometries, the magnet-on-cantilever geometry is discussed here since it can be used with a much more diverse set of samples.

The MRFM experiment seeks to measure the magnetic moment of spins in a sample by observing the deflection or frequency change of a magnet-tipped cantilever brought to within nanometers of the sample surface. A cross-sectional illustration of the experimental setup is sketched in Figure 1.1. A magnet extending beyond the leading edge of a cantilever is brought close to a sample containing nuclear or electron spins. Here the magnet is shown as a rectangular cuboid and the cantilever is aligned perpendicular to the sample surface. The magnet is magnetized along the direction of an external field \mathbf{B}^{ext} . A nearby microwave (MW) or radiofrequency (rf) source is used to manipulate electron or nuclear spins, respectively.

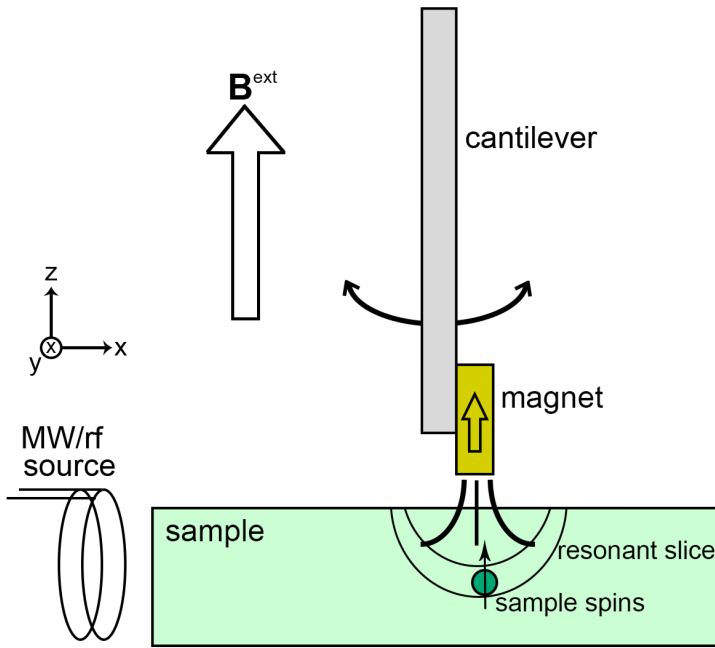


Figure 1.1: Schematic of a general MRFM experimental setup in the perpendicular or “pendulum” geometry. A rectangular cuboid magnet attached to a high-compliance cantilever is brought close to a sample surface. The magnet is magnetized in the direction of the external applied field $\mathbf{B}^{\text{ext}} = B_0 \hat{\mathbf{z}}$. A microwave/radiofrequency (MW/rf) source supplies a transverse magnetic field. The transverse magnetic field is used in combination with the distance-dependent field gradient supplied by the magnetic particle to manipulate the sample spins. The magnetization of the spins in a thin, bowl-shaped slice, called a resonant slice, is modulated to create an observable shift in the cantilever amplitude (for instance, the COZMIC [58] and cyclic-CERMIT [30, 59] protocols) or cantilever frequency (for instance, the CERMIT [55] protocol).

The MW/rf source is shown as a coil, but microwires [12, 48, 60], microstripline halfwave resonators [30], and coplanar waveguides [61] have also been used.

The force \mathbf{F} enacted between the magnetic moment of a spin $\boldsymbol{\mu}$ and the gradient of the magnetic field of a small magnetic particle \mathbf{B}^{tip} is

$$\mathbf{F} = (\boldsymbol{\mu} \cdot \nabla) \mathbf{B}^{\text{tip}}. \quad (1.1)$$

The magnetic particle is magnetized in the direction parallel to the applied external field, which we have defined as the z direction. The sample spins are also polarized in the direction of the applied external field such that μ_z is the only non-zero component of the spin magnetic moment.

The gradient-dipole force between the polarized spin magnetic moment μ_z and the magnetic particle is read out through the motion of a singly-clamped cantilever. The length of the cantilever can be aligned with respect to the nearby surface in two ways. In the first MRFM experiments, the cantilever was aligned parallel to the surface in the typical atomic force microscopy (AFM) geometry [14, 15, 52, 57, 62–65]. In the AFM geometry, the relevant field gradient is the vertical field gradient $\partial B_z^{\text{tip}} / \partial z$ and Eq. 1.1 can be simplified to

$$F_z = \mu_z \frac{\partial B_z^{\text{tip}}}{\partial z}. \quad (1.2)$$

More recently, ultrasensitive cantilevers [66–68] have been employed in MRFM experiments to detect smaller forces [25, 30, 53, 55, 56, 69–71]. Due to the high compliance nature of these cantilevers, a perpendicular “pendulum” geometry must be used instead of the AFM geometry to prevent the cantilevers from snapping into contact with the surface due to van der Waals interactions. The cantilever in Figure 1.1 is shown in the pendulum geometry. The relevant field gradient in the pendulum geometry is instead the lateral field gradient $\partial B_z^{\text{tip}} / \partial x$, which would lead to the gradient-dipole force being

$$F_x = \mu_z \frac{\partial B_z^{\text{tip}}}{\partial x}. \quad (1.3)$$

In the pendulum geometry, the net time-averaged force for a homogenously dispersed sample are equivalent on both sides of the cantilever, which results in no net force acting on the cantilever. New protocols were created in order to detect MRFM signal in the pendulum geometry. Two of these protocols include OSCAR (OScillating Cantilever Adiabatic Rapid passages) [52] and CERMIT (Cantilever-Enabled Readout of Magnetization Inversion Transients) [55]. OSCAR is a force-based MRFM protocol that is used to detect statistical imbalances in spin polarization; the OSCAR protocol has been used to detect statistical polarization of small ensembles of spins [56]. CERMIT, on the other hand, is a force-gradient-based protocol that can measure statistical imbalances [59] or can instead measure the interaction between the Curie law magnetization of large ensembles of spins and the second derivative of \mathbf{B}^{tip} [55]. Spin signal in a force-based MRFM experiment is measured by lock-in detection of a shift in the cantilever amplitude, whereas signal in a force-gradient-based MRFM experiment is observed as the change in the cantilever frequency before and after the spin magnetization is inverted. Note that unlike Curie law polarization, the net polarization due to statistical fluctuations carries random sign; thus, only the signal power — not the raw signal — can be averaged in the force-based OSCAR and Ref. 12 experiments.

In Chapter 5, a new force-based MRFM protocol based on the detection scheme used in Ref. 12 is introduced and used to measure the statistical fluctuations of a small ensemble of proton spins in a polystyrene film [58]. In this protocol, which is termed COZMIC (COmpensated Zero Mean Inversion Cycles), a frequency-chirped radiofrequency waveform was used to cyclically invert the proton magnetization at twice the resonance frequency f_c of the cantilever using adiabatic rapid passage [72] sweeps. The proton magnetization of the polystyrene film, which had a coherence time during rf modulation of $\tau_m \approx 0.1$ s, interacted with the field gradient of a rectangular cuboid nanomagnet to induce force fluctuations acting on the cantilever. Force fluctuations were measured in the COZMIC experiment instead

of the Curie law average polarization since the magnitude of the Curie law polarization was too small to be observed. Additional experimental details are provided in Section 5.2.4.

In MRFM experiments, imaging is achieved by applying a distance-dependent resonance condition to independently select spins in thin, bowl-shaped resonant slices [62]. The rf frequency f_{rf} at which resonance occurs for a given spin is dependent on both \mathbf{B}^{ext} and the distance-dependent field \mathbf{B}^{tip} supplied by the magnetic particle on the cantilever tip. The resonance condition is given by

$$f_{\text{rf}} = (\gamma/2\pi)|\mathbf{B}^{\text{ext}} + \mathbf{B}^{\text{tip}}(\mathbf{r})| \quad (1.4)$$

with γ the gyromagnetic ratio for the electron or nuclear spins and $\mathbf{B}^{\text{tip}}(\mathbf{r})$ the magnetic field generated by the magnetic particle at location \mathbf{r} . The gyromagnetic ratio for a proton spin is $\gamma_p/2\pi = 42.56 \text{ MHz/T}$ and for an electron spin is $\gamma_e/2\pi = 28 \text{ GHz/T}$. When protocols are implemented to invert the spin magnetization, only spins in or near the resonant slice are affected. By sweeping either \mathbf{B}^{ext} or f_{rf} , the spin density along the z -axis of the sample can be mapped. The thickness of the resonant slice is set by the sweep width and the intensity of the magnetic field gradient supplied by the magnetic particle.

For direct three-dimensional imaging, the process of sweeping through the sample thickness is iterated while laterally scanning along the x - and y -axes [12, 51, 73–75]. Spin density maps are obtained that can be used to reconstruct a three-dimensional image. The 4 nm resolution images produced by Degen *et al.* used the Landweber reconstruction algorithm [12]. The limitation of the Landweber algorithm is that it requires that the sample be of a finite size and that the spin density at all boundaries is zero. The algorithm worked well for the small tobacco mosaic virus particles studied in Ref. 12, but would introduce artifacts if the sample is larger than the image boundaries, such as when working with whole cells or photovoltaic devices. An alternative method was proposed by Kempf and Marohn to use Fourier-transform (FT) imaging to reconstruct images without introducing edge artifacts

[76]; two-dimensional FT imaging has been demonstrated by Nichol and Budakian for a polystyrene sample [77].

1.2 Dependence of MRFM Sensitivity on the Magnetic-Field Gradient and Force Fluctuations

The figure of merit to assess MRFM sensitivity is the achievable signal-to-noise ratio (SNR). In this section, we will consider the SNR for the COZMIC protocol implemented in Chapter 5. For stochastically-polarized proton spins in a force-based NMR-MRFM experiment, the power signal-to-noise ratio (SNR_p) is

$$\text{SNR}_p = \frac{N_{\text{spin}} \mu_p^2}{S_F} G_{zx}^2 \sqrt{T_{\text{avg}} \tau_m}, \quad (1.5)$$

with N_{spin} the number of spins in resonance, $\mu_p = 1.41 \times 10^{-26}$ N m T $^{-1}$ the proton magnetic moment, $G_{zx} = \partial B_z^{\text{tip}} / \partial x$ the lateral tip-field gradient, T_{avg} the signal averaging time, τ_m the spin correlation time, and S_F (in units of N 2 Hz $^{-1}$) the spectral density of force fluctuations experienced by the cantilever [78, 79]. Note that in Eq. 1.5, the “optimal reset-time theorem” introduced by Degen *et al.* to optimize the spin correlation time [70] was not taken into consideration.

Two parameters in Eq. 1.5 can be experimentally manipulated to improve the SNR per unit time for a given number of spins: the spin signal can be enhanced by achieving a high magnetic field gradient G_{zx} , and the noise can be minimized by working at low temperatures and having S_F approach the thermal limit. The parameters that influence S_F are considered in Section 1.2.1; optimizing the tip-field gradient is discussed in Section 1.2.2.

1.2.1 Minimizing Force Fluctuations for Magnet-Tipped Attoneutron-Sensitivity MRFM Cantilevers

The noise in an MRFM experiment is set by the spectral density of force fluctuations $S_F = (F_{\min}/b)^2$, with F_{\min} the minimum detectable force and b the detection bandwidth. F_{\min} is set by

$$F_{\min} = \sqrt{4k_B T (\Gamma_I + \Gamma_S) b} \quad (1.6)$$

with $k_B = 1.38 \times 10^{-23}$ N m K⁻¹ as Boltzmann's constant, T the experimental temperature, Γ_I the thermally-limited internal dissipation experienced by the cantilever due to thermal fluctuations, and Γ_S the surface-induced dissipation attributed to non-contact dielectric fluctuations.

The cantilever's thermally-limited dissipation, also known as the cantilever's "thermal floor", can be expressed in terms of the cantilever quality factor Q :

$$\Gamma_I = \frac{k}{2\pi Q f_c} = \frac{12.360}{14.064} \frac{wt^2}{Ql} (E\rho)^{1/2}, \quad (1.7)$$

with the cantilever spring constant $k = (1.030/4) E (wt^3/l^3)$ and the cantilever resonance frequency $f_c = (3.516/24\pi) t/l^2 (E/\rho)^{1/2}$ [68]. In these equations, w , t , and l are the width, thickness, and length of the cantilever beam; E is Young's modulus; ρ is the density; and $Q = \pi f_c \tau$ is the quality factor of the cantilever dependent on the cantilever ringdown time τ [68]. It can be determined from Eq. 1.7 that to minimize Γ_I , the cantilevers should be long, thin, and narrow. They also should be made of a material with a low Young's modulus and density while maintaining a high quality factor. Parameters that determine the quality factor are not fully understood, but are at least in part influenced by surface effects [66, 80]; a further discussion on the cantilever quality factor is provided in Section 3.3. All cantilevers used in the work presented in this thesis are made from single-crystal silicon, and the parameters for the fabricated cantilevers are $w = 4$ μm, $t = 340$ nm, $l = 200$ μm,

$E = 1.3 \times 10^{11} \text{ N m}^{-2}$, and $\rho = 2.3 \times 10^3 \text{ kg m}^{-3}$. The cantilevers are typically observed to have $k = 0.5$ to 1.0 mN m^{-1} , $f_c = 6$ to 9 kHz , and $Q = 40,000$ to $100,000$ [58, 81, 82].

As a high-compliance cantilever approaches a surface in the pendulum geometry, the friction experienced by the cantilever is observed to increase [83]. In MRFM experiments that detect the amplitude of the cantilever motion, such as the COZMIC protocol used in Chapter 5, minimizing the surface-induced dissipation Γ_S is critical. The strength of \mathbf{B}^{tip} is largest at small tip-sample separations, so Γ_S must be minimized for tip-sample separations as small as 5 nm. Over a polymer-coated surface, such as the polystyrene surface in Chapter 5, dielectric fluctuations in the polymer induce fluctuating electric fields that lead to damping interactions between the surface and the cantilever leading edge [84]. Mitigation of noncontact friction Γ_S for MRFM-style magnet-tipped cantilevers was studied extensively by Hickman *et al.* [81]. Surface-induced dissipation was minimized by reducing the cross-sectional area of the silicon near the cantilever leading edge and by extending a nanomagnet with a narrow cross-section past the leading edge of the silicon cantilever by at least 200 nm. It is important to note that the excellent Γ_S result of Ref. 81 was also due to the optimization of additional experimental parameters. In Ref. 81, the sample was chosen to be a thick layer of polystyrene that was coated with gold, and the potential of the cantilever was adjusted to null the contact potential difference between the gold-coated sample and the magnet-tipped cantilever. In a second experiment, no bias was placed on a similar overhanging magnet-tipped cantilever and an uncoated, 40 nm thick polystyrene sample was spin coated on a copper microwire [58]; additional experimental details are provided in Chapter 5. In the experiment in Ref. 58 and Chapter 5, significantly higher dissipation was observed than in the Ref. 81 experiment even though nearly identical overhanging magnet-tipped cantilevers were used. Instead of detecting the amplitude of cantilever motion, as in the COZMIC MRFM experiment, some MRFM protocols, such as OSCAR and CERMIT, detect shifts in the cantilever resonance frequency. The noise in frequency-based measurements is governed

by the power spectral density of cantilever frequency fluctuations $S_{\delta f_c}(f)$. The frequency fluctuations are set by

$$S_{\delta f_c} = 4k_B T \Gamma \left(\frac{f_c}{2k_c x_{\text{rms}}} \right)^2, \quad (1.8)$$

with Γ the total dissipation experienced by the cantilever and x_{rms} the root mean square (rms) amplitude of the cantilever motion. At low modulation frequencies f , additional sample-induced fluctuations $S_{\delta f_c} \propto f^{-1}$ are observed over polymer samples [85, 86]. At high modulation frequencies, the frequency fluctuations are dominated by detector noise $S_{\delta f_c} \propto f^2$ [85]. Frequency fluctuations are also very sensitive to mechanical vibrations [87].

Although the overhanging magnet-tipped cantilevers developed by Hickman *et al.* were shown to mitigate surface-induced dissipation, the frequency fluctuations measured when using these cantilevers were still quite large [58, 81]. A parametric upconversion scheme was developed and implemented in an MRFM experiment to convert a frequency-shift MRFM signal to an amplitude-detection signal [88]. Using this protocol, it should be possible to evade surface frequency noise and detector noise, and to instead be limited by Γ_s at close tip-sample separations.

1.2.2 Optimizing the Magnetic Field Gradient of Magnet-Tipped MRFM Cantilevers

In addition to minimizing cantilever dissipation, achieving a high SNR in an MRFM experiment requires that the magnetic particle exhibit a large magnetic field gradient. MRFM signal is maximized by using a magnet comprised of a material with a high saturated magnetic moment; the material's coercivity [89] and resistance to degradation [48] should also be taken into consideration. The magnet should be patterned to have a narrow cross-section, since the tip-field gradient — and thus the signal per spin in an MRFM experiment — scales

inversely with the size of the magnet. However, the cross-sectional area of an MRFM magnet should not simply be as small as possible. Instead, the optimal magnet cross-sectional area is dependent on the distance between the sample spin and the leading edge of the magnetic particle, also called the tip-sample separation h_{mag} . For example, let us consider the optimal magnet radius $r_{\text{mag}}^{\text{opt}}$ for a magnet that is approximated as a uniformly magnetized spherical particle. Under the assumption that the MRFM signal is due to force detection of a single spin [17], the optimal magnet radius is

$$r_{\text{mag}}^{\text{opt}} = 3h_{\text{mag}}. \quad (1.9)$$

Eq. 1.9 also holds true in a force-gradient experiment on a single spin when the cantilever amplitude is set to an optimal value [17]; optimizing the detection of multiple spins in a force-gradient experiment has been considered by Lee and coworkers [90].

A key implication of Eq. 1.9 is that there is not a single optimal magnetic particle width. The tip-sample separation is based on the sample spin's depth below the sample surface; therefore, $r_{\text{mag}}^{\text{opt}}$ also is dependent on the sample spin location. For instance, if the distance between the magnet leading edge and the sample surface is 5 nm and if spins are detected within the top 50 nm of the top of the sample, $r_{\text{mag}}^{\text{opt}}$ would range from 15 to 165 nm. Thus, Eq. 1.9 indicates that the fabrication of MRFM magnets should allow for the patterning of magnets with easily tunable dimensions.

Optimizing the tip-sample separation requires consideration of how both the signal and noise in an MRFM experiment are influenced by h_{mag} . MRFM signal increases as h_{mag} is reduced; however, MRFM measurement noise — which is set by the spectral density of force fluctuations S_F , and specifically by the surface-induced dissipation Γ_S — also increases as the distance between the cantilever leading edge and the sample surface is reduced. Thus, maximizing the SNR in an MRFM experiment requires setting h_{mag} as small as possible while still maintaining S_F within acceptable limits.

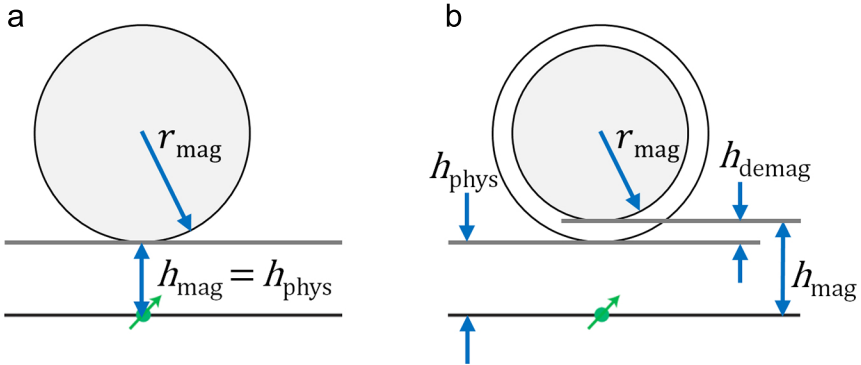


Figure 1.2: Cross-sectional schematics of spherical magnets demonstrate the influence of magnetically inactive “damage” layers on the tip-sample separation h_{mag} . (a) Fully-intact magnet (gray circle) with radius r_{mag} . The distance between the sample spin (green arrow) and the leading edge of the magnetic material h_{mag} is the same as the physical separation h_{phys} . (b) Magnet with a damage layer of thickness h_{demag} . For the damaged magnet, $h_{\text{mag}} = h_{\text{phys}} + h_{\text{demag}}$.

Two additional factors must be considered to achieve the highest MRFM signal. To minimize h_{mag} for a given separation between the cantilever leading edge and the sample surface, the leading edge of the magnet should be in line with, or overhanging, the leading edge of the cantilever. Once the optimal h_{mag} is determined, potential magnetic damage layers also must be considered. As shown in Figure 1.2, a “damage” layer of demagnetized material with thickness h_{demag} at the magnet edge would increase the spacing between the sample spin and the magnetic material in the nanomagnet. Instead of h_{mag} being equal to the physical spacing h_{phys} between the sample spin and the physical leading edge of the magnet, the introduction of a damage layer would increase the tip-sample separation to $h_{\text{mag}} = h_{\text{phys}} + h_{\text{demag}}$. Due to the increase in h_{mag} , magnets with a damage layer exhibit lower observable tip-field gradients.

The focus of Chapters 2 through 5 in this thesis is the preparation of high-gradient nanomagnet-tipped cantilevers. Nanomagnets with adjustable dimensions are defined using electron beam (e-beam) lithography and deposited using e-beam evaporation; this combination of techniques can produce nanomagnets with cross-sectional areas ranging from

$200 \times 200 \text{ nm}^2$ to less than $30 \times 30 \text{ nm}^2$. The key constraint during nanomagnet fabrication is prevention of the formation of magnetically inactive layers at the nanomagnet leading edge. In this thesis, the minimization of damage layers is achieved by careful process integration and limiting degradation due to chemical and heat-induced damage.

1.3 Outline of the Dissertation

The work in this thesis centers on the development of a method to fabricate high-gradient nanomagnets attached to cantilevers. As discussed in Sections 1.2.1 and 1.2.2, high-resolution imaging can only be achieved by combining (1) large per-spin signal resulting from high field gradients and (2) low Γ_I and Γ_S noise due to the thermal fluctuations in the cantilever and noncontact surface dissipation, respectively. To that end, a second design criteria for high sensitivity in MRFM is to overhang the nanomagnet past the leading edge of the cantilever, both to reduce the noncontact friction, as observed in Ref. 81, and to have the leading edge of the nanomagnet as close to the sample spins as possible. It is furthermore essential to minimize magnetic damage, particularly at the nanomagnet leading edge. Since previous efforts to fabricate nanomagnets on cantilevers [25, 53, 54, 56, 57] resulted in tip-field gradients that were almost an order of magnitude smaller than the tip-field gradients needed for nanometer-scale NMR-MRFM imaging [12], it is essential to develop a new protocol to fabricate high-gradient nanomagnets on cantilevers.

Chapter 2 begins with a summary of the prior approaches for the fabrication of magnets on cantilevers and a discussion of the record-low dissipation for a cantilever with an integrated nickel nanomagnet that was observed by Hickman *et al.* [81]. My attempts to reproduce the Hickman fabrication protocol indicated that the yield for the magnet-tipped cantilevers was extremely low. I report new findings that indicate that the low yield of the Hickman protocol

was due to a combination of exceeding the thermal budget for the nanomagnets and damage during deposition of plasma enhanced chemical vapor deposition of silicon dioxide. Attempts to improve the yield and magnetization of the magnet-tipped cantilevers, including the use of barrier layers, are described. The chapter concludes with a discussion of alternative methods to attach magnetic particles to cantilevers.

Chapter 3 introduces a new fabrication protocol that was designed to improve the process yield, decrease processing-induced damage, and retain the critical ability to use high-resolution electron beam lithography to define the nanomagnets. The protocol involves a combination of batch- and serial-fabrication processing. Magnets are defined on a silicon-on-insulator wafer using e-beam lithography and liftoff. The wafer is then batch-processed to yield nanomagnet tips protruding from the leading edge of suspended micron-scale silicon chips, which are attached serially to the ends of attonewton-sensitivity silicon cantilevers using focused ion beam (FIB) milling and attachment. Methods for fabricating nickel and cobalt nanomagnet-tipped chips, and for conducting the FIB lift-out procedure, are described. Optimization of the experimental parameters and alternative fabrication methods are discussed. The successful fabrication of cobalt nanomagnets, which has a saturation magnetization that is $3\times$ larger than nickel, is a particularly exciting advance since previous attempts to batch-fabricate cobalt nanomagnets had been unsuccessful [91].

Chapter 4 describes extensive characterization of the elemental composition and magnetization of nickel and cobalt thin films. Frequency-shift cantilever magnetometry was conducted to assess the saturated magnetic moment of individual nickel and cobalt nanomagnets. Large-area thin films of both nickel and cobalt were characterized by superconducting quantum interference device (SQUID) magnetometry. SQUID magnetometry conducted on both uncapped and platinum-capped films indicated that the magnetic material saturated near the theoretical values. X-ray photoelectron spectroscopy (XPS) with depth profiling

was conducted on both uncapped and platinum-capped thin films of nickel and cobalt to determine the extent of oxidation damage; XPS findings indicated that unprotected magnetic materials incurred less than 10 nm of oxidation, and that oxidation was prevented by capping with 10 nm of platinum.

Chapter 5 details the use of an attonewton-sensitivity cantilever with an integrated cobalt nanomagnet tip to detect NMR-MRFM signal with ≤ 500 proton magnetic moment sensitivity. Spin signal was obtained at tip-sample separations ranging from 13.1 nm to 42.3 nm. The observed tip-field gradient of 4.4 to 5.4MTm^{-1} is comparable to the 4.2MTm^{-1} field gradient produced by the Fe₇₀Co₃₀ pillar in the sample-on-cantilever experiment of Ref. 12 and is 8 to 10 times larger than the best tip-field gradient demonstrated to date in a magnet-on-cantilever MRFM experiment [53]. For the closest tip-sample separation of 13.1 nm and under the signal averaging conditions of Ref. 12, these magnet-tipped cantilevers are projected to achieve a resolution of 5 to 10 nm. The resolution could be further improved by minimizing the noncontact friction, which was significantly higher than what had been observed by Hickman *et al.* [81]. It is hypothesized that Γ was dominated by eddy current damping in this experiment, which could be mitigated by increasing the thickness of the sample or putting a bias on the cantilever to null the contact potential difference between the tip and the substrate.

Chapter 6 discusses the development of Cornell's third-generation magnetic resonance force microscope, which will be used to conduct high-resolution three-dimensional MRFM imaging experiments. The key enhancement is that this microscope has a stage with three dimensions of motion. Other improved features include superior vibrational isolation, a longer hold time for the liquid helium dewar containing the 9 T superconducting magnet, separate coaxial lines for radiowaves and microwaves, and enhanced heat sinking of the probe head.

Chapter 7 summarizes the key findings in this dissertation and comments on potential future directions for the fabrication of magnet-tipped cantilevers with further improved performance.

Work presented in this thesis includes findings that were previously published in three manuscripts (Refs. 81, 82, and 58), in addition to extensive newly-presented results. The publication status of the work in the chapters of this thesis is summarized in this paragraph; copyright information for previously-published figures is detailed in each chapter. Scanning transmission electron microscopy (STEM) and electron energy loss spectroscopy (EELS) data for an integrated nickel nanomagnet on cantilever (Section 2.3) were published in Ref. 81. The original nickel magnet-tipped chip fabrication protocol (Section 3.2), FIB lift-out procedure (Section 3.4), and details on process optimization (Sections 3.5, 3.7.2, and 3.8) were first reported in Ref. 82. The fabrication of cobalt magnet-tipped chips (Section 3.6) and improved FIB lift-out procedure (Section 3.7.1) were introduced in Ref. 58. For magnetic-material characterization, the nickel frequency-shift cantilever magnetometry data (Section 4.1) were published in Ref. 82, and the cobalt cantilever magnetometry (Section 4.4) and large-area thin-film cobalt SQUID magnetometry and XPS findings (Section 4.3) were presented in the manuscript and Supporting Information of Ref. 58. All data presented in Chapter 5 were published in Ref. 58. The work presented here for the first time includes the vast majority of Chapters 1, 6, and 7; all data in Chapter 2 aside from Figures 2.2(c,e), 2.5, and 2.7; additional figures and details to clarify the methods discussed in Chapter 3; and the SQUID and XPS findings for nickel thin films in Section 4.3. The work conducted in this thesis was carried out with collaborations and funding that are acknowledged separately at the end of each chapter.

CHAPTER 2

MAGNET-ON-CANTILEVER PRECEDENT AND INTEGRATED MAGNET-ON-CANTILEVER FABRICATION

2.1 Introduction

The development of attonewton-sensitivity cantilevers [66, 68] has opened up exciting new approaches for characterizing materials. Attонewton-sensitivity cantilevers have been used to detect electron spin resonance (ESR) [25, 30] and nuclear magnetic resonance (NMR) [12, 55], to observe near-surface dissipation due to dopants in semiconductors [92] and dielectric fluctuations in polymers [84, 86], to characterize switching and fluctuations of ferromagnetic domains in individual magnetic nanoparticles [68, 89, 93] and individual magnetic vortices in superconducting rings [94], and to measure persistent currents in normal metal rings [95, 96].

The application of studying ESR or NMR in an MRFM experiment requires that an attonewton-sensitivity cantilever be functionalized with either a sample [12, 48, 70, 71] or a magnetic particle [25, 30, 53, 55, 56, 68, 69, 89, 92, 93]. Although the interaction between the magnetic moment of the sample spins and the field gradient of the magnetic particle is independent of which component is adhered to the cantilever, other factors strongly influence the choice between the magnet-on-cantilever and sample-on-cantilever geometries. The key consideration for determining the MRFM geometry is the sample of interest. As discussed in Chapter 1, the preparation methods required for many exciting samples are incompatible with the limitations of working at the leading edge of an attonewton-sensitivity cantilever. Thus, to study the widest range of samples in MRFM experiments, it is critical to prepare the sample off-cantilever and instead attach the magnet to the cantilever.

In Chapter 3 a new combination batch- and serial-fabrication protocol for the fabrication

of magnet-tipped cantilevers will be introduced. Using the Chapter 3 approach, magnets are batch-fabricated on microscale silicon chips and are serially adhered to separately-prepared attonewton-sensitivity cantilevers. Cobalt nanomagnets fabricated using this combined batch-and-serial technique are ultimately shown to exhibit the highest tip-field gradients to date for the magnet-on-cantilever geometry.

In order to motivate the development of the magnet-on-cantilever fabrication protocol presented in Chapter 3, it is critical to understand the limitations of previous integrated magnet-on-cantilever methods. Section 2.2 includes a summary of the previous methods used in the MRFM community to fabricate integrated magnets on cantilevers. The protocol introduced by Hickman *et al.* [81] best met the criteria discussed in Section 1.2.2 for the optimal magnet design for magnet-tipped MRFM cantilevers. However, the yield of the Hickman protocol was not reported, and attempts to reproduce the procedure had extremely low yields of < 1%. In Sections 2.3 and 2.4, characterization of the failure mechanism of the Hickman fabrication protocol is discussed and attempts to improve the process yield through the introduction of barrier layers to prevent oxidation and silicidation of the magnetic material, which proved to be unsuccessful, are described. The work presented in this chapter is summarized in Section 2.5, and in Section 2.6 is a discussion of the goals for the new high-yield fabrication protocol detailed in Chapter 3.

2.2 Prior Magnet-on-Cantilever Fabrication Methods and Results

The force of the interaction between the magnetic moment of a single electron spin and the magnetic field gradient of a small cobalt ferromagnet (approximated as a spherical particle of radius 50 nm) with $h_{\text{mag}} = 10 \text{ nm}$ is on the order of $10^{-16} \text{ N} = 100 \text{ aN}$; the force due to the interaction between a single proton and the same magnetic particle is three orders

of magnitude lower with a force of approximately 0.1 aN [66, 97]. In a joint experiment by Kenny’s group at Stanford University and Rugar’s team at IBM Almaden Research Center, Stowe *et al.* introduced the first protocol to fabricate cantilevers with sufficient sensitivity to detect attonewton-scale forces [66]. The cantilevers were prepared by thinning the device silicon layer of a silicon-on-insulator (SOI) wafer to as thin as 50 nm, followed by defining the cantilever bodies and sharp leading-edge tips using two overlapping optical lithography masks. After backside processing, cantilevers up to 400 μm long and as thin as 60 nm were released using critical point drying, with yields higher than 80%. The cantilevers exhibited a spring constant as low as $6.5 \times 10^{-6} \text{ N m}^{-1}$ and a minimum detectable force $F_{\min} = 5.6 \text{ aN}$ in a 1 Hz bandwidth at a temperature of 4.8 K. However, the cantilever quality factor Q at 4.8 K was only $Q = 6,700$. In comparison to $Q = 26,000$ for similarly-prepared 175 nm thick cantilevers, the relatively low Q for these 50 nm thick cantilevers indicated that surface effects induced significant cantilever energy losses. In Ref. 66, magnetic tips were prepared on individual attonewton-sensitivity cantilevers using shadow-masked evaporation of cobalt onto the sidewalls of post-released cantilevers. In order to evaporate metal on the sidewall of the cantilever leading edge, each cantilever was loaded into the evaporator at an angle with respect to the cobalt target, and the majority of the cantilever was masked off using a knife edge. The magnet-tipped cantilevers of Ref. 66 were not used in an MRFM experiment.

Chui *et al.* extended the Stowe fabrication protocol during a second collaboration between the Kenny and Rugar groups [98]. In the revised process, the cantilevers were mass-loaded at the leading edge to damp high-order modes of the cantilever and mitigate high-frequency vibrational noise [99, 100]. The thickness of the base of the cantilevers was also increased to minimize clamping losses from misalignment of the front and back sides of the cantilever handle chips. The bendable “hinge” portion of the cantilever was fabricated from the 100 nm thick single-crystal silicon device layer of SOI wafers, and the added thicknesses of the mass loaded cantilever leading edge and cantilever base were achieved by two separately-masked

undoped single-crystal silicon epitaxial growths. The thickness of the mass-loaded cantilever leading edge was 2 μm , and the base of the cantilever was grown to a thickness of 5 μm . The cantilevers were then fabricated in a manner similar to Ref. 66. The cantilever quality factor, spring constant, and resonance frequency were observed to be up to $Q = 80,000$ (at 20 K), $k = 3 \times 10^{-4} \text{ N m}^{-1}$, and $f_c = 7 \text{ kHz}$, respectively; using Eqs. 1.6 and 1.7, Q , k , and f_c can be used to calculate that the corresponding $F_{\min} = 10 \text{ aN}$ in a 1 Hz bandwidth at $T = 20 \text{ K}$. To use the magnet-on-cantilever geometry in subsequent MRFM experiments, samarium cobalt (SmCo) magnetic particles were serially attached to the leading edge of the mass-loaded cantilevers. To improve the tip-field gradient exhibited by SmCo magnets, the width of the particles was reduced to as small as 150 nm using focused ion beam (FIB) milling [25]; due to FIB-milling-induced magnetic damage, the particle width could not be further reduced. The largest vertical and lateral tip field gradients reported by FIB-milling of SmCo magnets employed in MRFM experiments were $\partial B_z^{\text{tip}}/\partial z = 5.5 \times 10^5 \text{ T m}^{-1}$ and $\partial B_z^{\text{tip}}/\partial x = 4.3 \times 10^5 \text{ T m}^{-1}$, respectively [53]. For reference, the tip-field gradients used in the high-resolution MRFM imaging experiment of Ref. 12, which used the sample-on-cantilever geometry, were an order of magnitude larger. Although one of the SmCo-tipped cantilevers was used to detect ESR-MRFM signal from a single electron spin in the seminal experiment of Ref. 25, 13 hours of signal averaging were required per point. It thus was unfortunately determined that FIB-milled SmCo-tipped cantilevers produced insufficient tip-field gradients for high-resolution MRFM imaging experiments.

Methods to batch fabricate integrated nanomagnets directly on attonewton-sensitivity cantilevers were investigated by Marohn's group at Cornell University. In 2004, Jenkins *et al.* batch-fabricated nickel nanomagnets as small as $1.2 \mu\text{m} \times 400 \text{ nm}$ in area and 200 nm thick using electron-beam (e-beam) lithography and thermal evaporation [68]. Cantilevers were defined around the pre-deposited magnets such that the magnets were near the cantilever leading edge. The cantilevers were fabricated from the 340 nm thick device silicon layer of SOI

wafers. The cantilever fabrication and release process followed the methods of Ref. 66. The magnet-tipped cantilevers were not employed in a magnet-on-cantilever MRFM experiment, but frequency-shift cantilever magnetometry results indicated that the magnets were close to fully magnetized and had a damage layer of less than 28 nm. At a temperature of approximately 11 K, quality factors were observed to be as high as $Q = 200,000$, indicating that the surface effects observed by Stowe *et al.* in Ref. 66 had been minimized.

Although F_{\min} is set by the intrinsic dissipation and experimental temperature at large tip-sample separations, as shown in Eq. 1.6, at small tip-sample separations F_{\min} is often dominated by surface interactions. In an effort to maintain low F_{\min} at close tip-sample separations, Hickman *et al.* revised the Jenkins magnet-on-cantilever batch-fabrication protocol to extend e-beam-defined nickel nanomagnets past the leading edge of attonewton-sensitivity cantilevers [81]. The observed cantilever spring constants for the magnet-tipped cantilevers were approximately $8 \times 10^{-4} \text{ N m}^{-1}$. Q varied significantly between cantilevers, ranging from 85,000 to as high as 235,000. The key alteration in the Hickman protocol, the overhanging nature of the nanomagnet, was expected to minimize surface-induced dissipation by improving the spatial separation between trapped charge on the silicon cantilever and electric field fluctuations in the substrate. It was observed that the overhanging nickel-tipped cantilevers did in fact exhibit a record-small force sensitivity for a magnet-tipped cantilever near a surface. At a temperature of 4.2 K, $F_{\min} < 10 \text{ aN}$ ($b = 1 \text{ Hz}$ bandwidth) for tip-sample separations down to 3 nm [81]. For comparison, $F_{\min} = 10 \text{ aN}$ was observed at a tip-sample separation of 24 nm in the 4 to 10 nm resolution NMR-MRFM imaging experiment of Ref. 12. The nickel nanomagnets were characterized by cantilever magnetometry and found to have saturation magnetizations that were roughly 70% of the theoretical value. However, when the nickel magnet-tipped cantilevers were used in an MRFM experiment, the experimentally observed ESR-MRFM signal had poor agreement with theory. The same theory gave a predicted signal that agreed almost perfectly with the observed signal in an ESR-MRFM experiment

that used a 4 μm diameter spherical nickel magnet-tipped cantilever [30], indicating that the nickel nanomagnets fabricated using the Hickman protocol were not as well-magnetized as expected.

Out of these prior methods developed for magnet-tipped cantilevers in MRFM experiments, the fabrication protocol introduced by Hickman *et al.* best meets the criteria described in Section 1.2.2 for defining reproducible, adjustable, and small-scale magnets on cantilevers that experience minimal force sensitivity degradation as the tip-sample separation is reduced. Additionally, Hickman *et al.* demonstrated that overhanging the magnet past the cantilever leading edge produced cantilevers that could be brought to within less than 5 nm of the sample surface without significantly increasing the surface-induced dissipation. Unfortunately, the yield of the Hickman process was low and the magnets prepared by Hickman were not well-magnetized. In Sections 2.3 and 2.4, efforts to reproduce and improve the Hickman fabrication protocol are discussed.

2.3 Process Integration Challenges of the Overhanging Nanomagnet-on-Cantilever Fabrication Protocol

The key steps of the Hickman protocol are shown in Figure 2.1. The process is fully described in Refs. 81 and 91; an overview of the critical components of the process is provided here to facilitate subsequent discussion of the low yield and failure mechanism. SOI wafers with a 340 nm thick, $\langle 100 \rangle$ oriented device silicon layer and a 400 nm thick buried oxide (BOX) silicon dioxide (SiO_2) layer were used. Platinum alignment marks were used to align subsequent e-beam lithography and photolithography steps; the 100 nm thick marks were defined using e-beam lithography and evaporated using e-beam evaporation (with a 5 nm thick chromium adhesion layer). Nickel nanomagnets as narrow as 100 nm in width were de-

fined in bilayer resist [101] by e-beam lithography and were deposited by e-beam evaporation (Figure 2.1, Step 2). A 5 nm chromium layer was deposited under the nickel magnets to promote adhesion to the silicon substrate. U-shaped holes were defined by e-beam lithography and a calibrated isotropic SF₆:O₂ reactive ion etch (RIE) plasma etch was used to remove the silicon under the magnet leading edge to create a 100 to 300 nm overhang (Figure 2.1, Step 3 and Inset A). The cantilever bodies were patterned using photolithography and an identical SF₆:O₂ silicon plasma etch (Figure 2.1, Step 4 and Inset B). Prior to backside processing, the front and back of the wafer were coated with low-stress plasma enhanced chemical vapor deposition (PECVD) SiO₂ at 275°C (Figure 2.1, Step 5); the front of the wafer was coated first with 1.6 μm of PECVD SiO₂ to protect the magnets and cantilevers against damage, and the backside was coated afterwards with 2 μm of SiO₂ that was used as an etch mask during subsequent steps. Windows in the wafer substrate under the cantilevers were defined in photoresist on the back side of the wafer, and the pattern was transferred to the backside SiO₂ using a CHF₃:O₂ etch (Figure 2.1, Step 6). The 500 μm thick handle silicon layer was anisotropically etched using deep reactive silicon etching, commonly called Bosch etching (Figure 2.1, Step 7) [102]. The backside photoresist acted as the etch mask while etching the first 400 μm of the handle silicon layer; prior to etching the final 100 μm of handle silicon, the resist was stripped, leaving the backside SiO₂ as the only remaining etch mask. A “handler” wafer [91] also was attached to the device side of the wafer prior to etching the final 100 μm of handle silicon. Because the Bosch etching tool flows helium gas over the back of the wafer to keep the substrate cool during processing, an air-tight seal between the tool and the wafer must be retained at all times. When the windows in the device wafer become very thin membranes, they are subject to cracking; the handler wafer was attached to the helium-cooling side of the wafer to retain an air-tight seal in the Bosch tool even if the membranes cracked. Since adding the handler wafer reduced the cooling efficiency while the handle wafer was attached, the wafer was frequently removed from the

etch chamber to cool. To release the cantilevers, the PECVD and BOX SiO₂ layers were simultaneously etched using buffered oxide etch (BOE); the thickness of the PECVD SiO₂ had been set so that it would release at the same time as the BOX SiO₂ layer in order to limit exposure of the magnetic material to BOE. The cantilevers were critical point dried to prevent curling or stiction (Figure 2.1, Step 8). Overall, the Hickman fabrication protocol required 38 fabrication steps on 10 different fabrication tools and instruments; the process could be completed with approximately two weeks of processing time.

The yield of the original Hickman fabrication protocol was not reported, but magnetic material damage to a significant number of the nickel nanomagnets was discussed in Ref. 91. Tentative evidence indicated that the nickel magnets were converted to nickel silicide during the through-wafer Bosch etch — particularly while the handler wafer was attached — due to an increased temperature of the substrate; efforts were made to minimize the damage by removing the wafer from the etch chamber frequently to cool. However, conclusive evidence confirming the damage mechanism was not reported, and it remained unclear whether the damage was due to poor process control or a fundamental incompatibilities due to poor process control or chemical reactions between silicon, chromium, and nickel at the high temperatures present during backside etching.

New work was undertaken to determine the yield of the Hickman protocol and to better understand the sources of nanomagnet damage. Attempts to reproduce the Hickman protocol were conducted on four separate wafers. Scanning electron microscopy (SEM) images from three of these iterations are presented in Figure 2.2.¹ Images are shown for magnets at the completion of the front-side processing (Figure 2.2(a,b)) and at the end of the process after the cantilevers were released (Figure 2.2(c-h)). It was observed that although most magnets were still intact after the completion of the front-side processing, less than 1% of

¹Figure 2.2(c,e) reprinted with permission from J. G. Longenecker *et al.*, *J. Vac. Sci. Technol. B* **29**, 032001 (2011). Copyright 2011, American Vacuum Society.

Device Silicon Buried Silicon Oxide Bulk Silicon Resist Nickel Protective Oxide

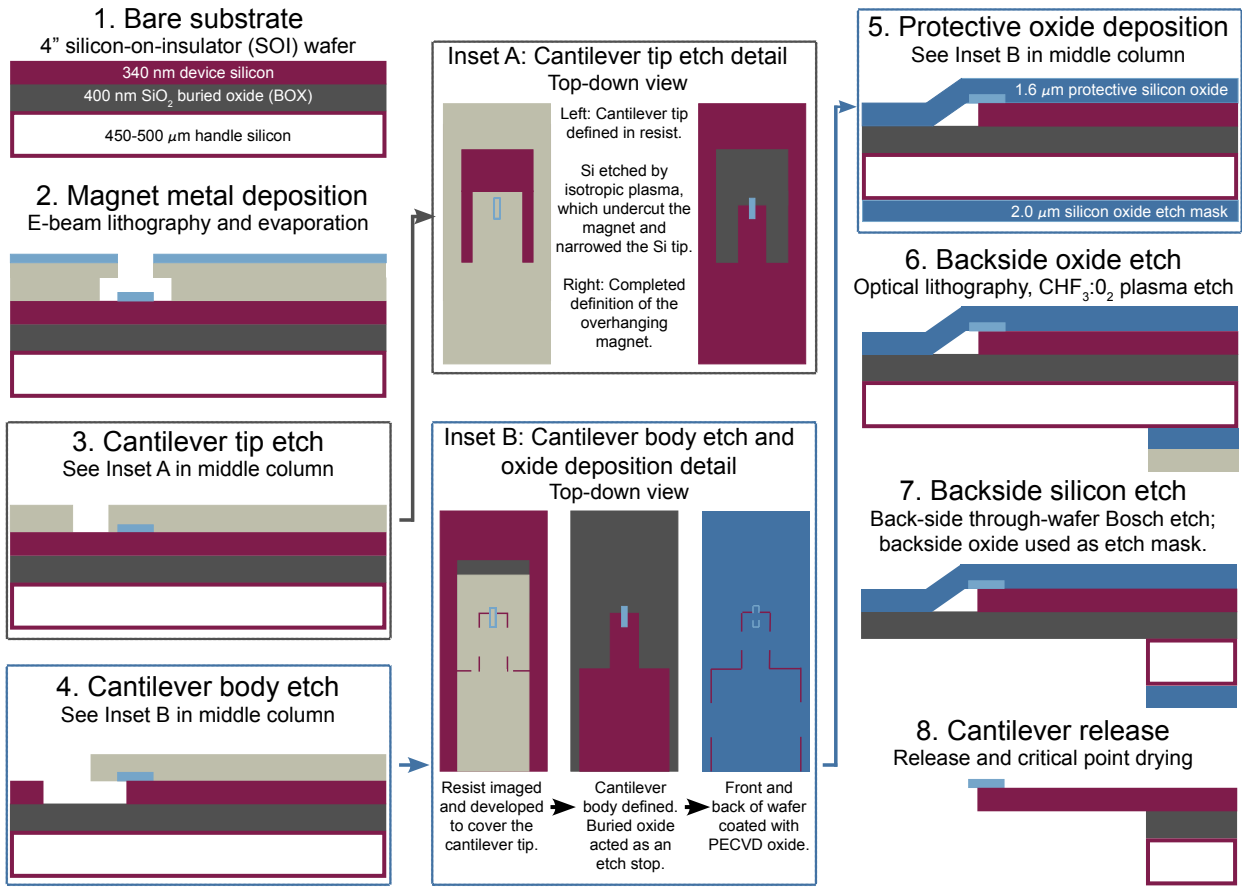


Figure 2.1: Schematics of the key steps of the integrated, overhanging magnet-tipped cantilever fabrication protocol introduced by Hickman *et al.* [81]. The color key is provided at the top of the image. (1) SOI wafers with a 340 nm thick device silicon layer and 400 nm thick buried oxide (BOX) layer were used. (2) 100 nm thick nickel nanomagnets, with a 5 nm chromium adhesion layer, were defined in bilayer resist by e-beam lithography and deposited by e-beam evaporation; the resist was lifted off after deposition. (3) U-shaped holes (top-down view schematic in Inset A, left side) directly above the nanomagnets were defined using e-beam lithography. The silicon device layer was isotropically etched using SF₆:O₂ plasma to achieve a magnet overhang of 300 nm and reduce the width of the silicon at the leading edge; a top-down view of the magnet overhang after the resist was stripped is shown in the right-hand image in Inset A. (4) The cantilever bodies were defined using photolithography and were etched using an SF₆:O₂ plasma (before and after top-down views of Step 4 are shown in the left and middle images of Inset B). (5) PECVD SiO₂ was deposited on the top and bottom sides of the wafer. (6) Windows in the wafer substrate under the cantilevers were defined in photoresist, and the exposed PECVD SiO₂ was etched using CHF₃:O₂ plasma. (7) The silicon handle wafer was anisotropically etched using through-wafer Bosch etching. (8) The cantilevers were released by using BOE to etch the BOX and PECVD SiO₂ layers, and the cantilevers were critical point dried to prevent stiction.

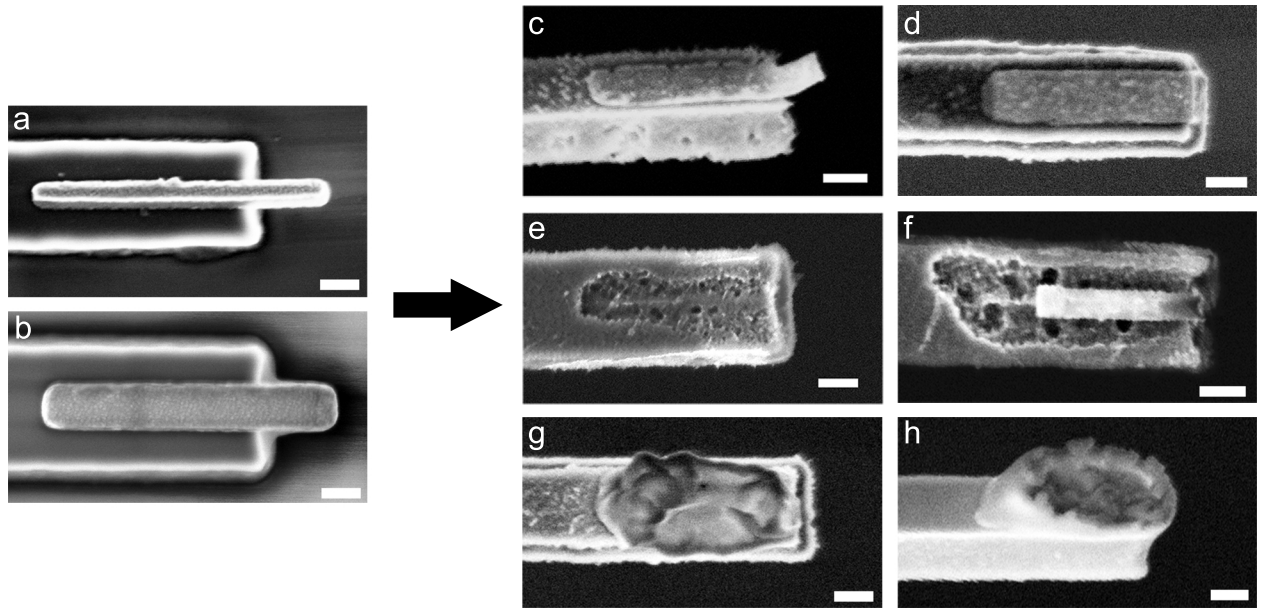


Figure 2.2: SEM images of nickel nanomagnets at the leading edge of attonewton-sensitivity cantilevers. (a,b) Nickel magnets remained intact after the completion of the front-side cantilever definition (Step 4 in Figure 2.1). (c-h) Nickel magnets were extensively damaged at the end of the process. Common damage scenarios consisted of partial or complete damage to the magnet leading edge (c,d), damage involving the removal of silicon near the nanomagnet (e,f), or the alteration of the nickel structure (g,h). All scale bars represent 200 nm.

magnets survived the remainder of the process. Multiple damage scenarios were observed: the magnetic material at the leading edge of the magnets was damaged (Figure 2.2(c)) or missing (Figure 2.2(d)); device layer silicon surrounding the nanomagnets was removed and the nickel nanomagnets were completely (Figure 2.2(a)) or partially (Figure 2.2(b)) missing; or, the nickel material reacted to form an unknown amorphous compound (Figure 2.2(g,h)). It was extremely difficult to explore the mechanism(s) leading to this extensive damage since, to avoid physical damage during backside processing, the magnets and cantilevers were encased in PECVD SiO₂ after the cantilever definition; after the protective PECVD SiO₂ was deposited, the magnets could not be visualized until the cantilevers were released.

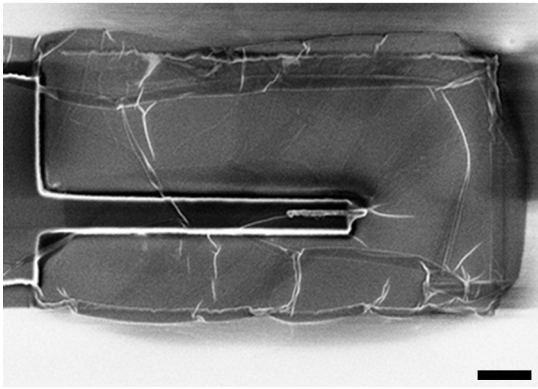
The formation of nickel silicide can account for some of the observed damage in Figure 2.2. During deposition of the nickel magnetic material, the 1.5 nm thick native SiO₂ layer on the

silicon substrate [103], coupled with a chromium or titanium adhesion layer, is sufficient to prevent the formation of nickel silicide. However, nickel silicide readily forms on Si⟨100⟩ substrates at temperatures above 250°C [104, 105]; the nickel-rich Ni₂Si phase is formed at 250–350°C, and increasingly silicon-rich phases are observed above 350°C. There are two processing steps when the nickel nanomagnets were exposed to temperatures above 250°C in the Hickman fabrication protocol: (1) during the 275°C PECVD SiO₂ deposition on the front and back sides of the wafer, and (2) during the through-wafer Bosch etch. Although helium cooling should prevent temperature spikes during Bosch processing, the helium flow is insufficient to cool the wafer once the handler wafer is attached, and it is likely that the temperature exceeds 300° [106]. The damage observed in Figure 2.2(g,h) thus can be attributed to the formation of nickel silicide. However, it is unlikely that the formation of nickel silicide accounts for the damage to the nanomagnets that are partially or completely missing after the release in BOE, since nickel silicide is resistant to etching by hydrofluoric acid/BOE [107].

The remainder of the damage observed in Figure 2.2 required another mechanism. Other than the silicon substrate and the chromium adhesion layer, the only chemicals that the nickel was exposed to directly were the silane (SiH₄) and nitrous oxide (N₂O) precursors for the PECVD SiO₂ deposition. By concurrent exposure to a plasma and elevated temperatures of 275°C, it is likely that these PECVD SiO₂ precursors could react with the nickel nanomagnets. Silane has been shown to dissolve into nickel at temperatures above 125°C [108], and decomposed precursors that form reactive oxygen species could oxidize the nickel beyond the typical 3 nm NiO thickness [109–112] observed at temperatures up to 275°C.

Evidence that interactions between unprotected nickel nanomagnets and the PECVD SiO₂ precursors contributed to the damage observed in Figure 2.2 was obtained during the fourth iteration of reproducing the Hickman fabrication protocol. For this wafer, a film

a) Before backside processing



b) After cantilever release

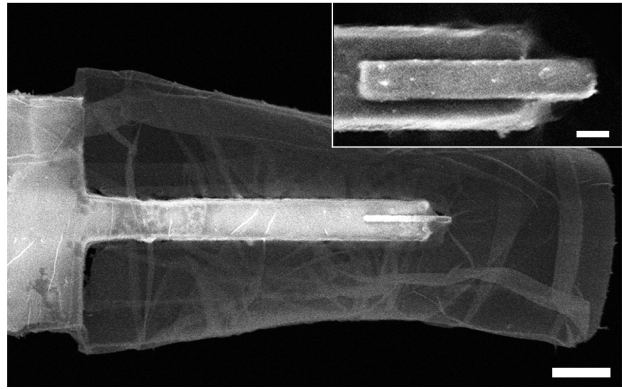


Figure 2.3: SEM images of the leading edges of magnet-tipped cantilevers that were coated with a thin film, likely residual photoresist. (a) Magnet-tipped cantilever after the cantilever bodies were etched (Step 4 in Figure 2.1) and the photoresist strip processing step had been conducted. However, the SEM image indicates that the resist had not lifted off properly. (b) The leading edge of a magnet-tipped cantilever after release. The thin film was still present on most cantilevers, with visually intact magnets underneath. The film had lifted off of a few of the magnets during the release; one of these film-free magnets is shown in the inset. The scale bars in (a) and (b) represent 1 μ m, and the scale bar in the inset represents 200 nm.

remained over the cantilevers and magnets after the front-side photolithography step used to define the silicon cantilever bodies (Figure 2.3(a)); the film was likely residual photoresist. Although film-coated cantilevers would be unsuitable for MRFM experiments, the processing of the wafer was still completed. It was observed that unlike the other trials, most of the film-coated magnets remained intact after processing (Figure 2.3(b)); the residual film even lifted off of some magnets during release, leaving a few magnets that were film-free and largely intact (Figure 2.3(b) inset). The only known difference between the first three iterations of the Hickman protocol, in which almost all magnets were damaged, and the fourth trial, when many magnets remained intact, is that the magnets for the fourth trial were inadvertently protected during the PECVD deposition. This observation suggests that in addition to silicide damage, the magnets were also damaged by the PECVD SiO₂ processing step.

The integrity of one of the nickel nanomagnets that had remained intact during the fourth iteration of reproducing the Hickman protocol, and was not coated with resist after

the release of the cantilever, was assessed by scanning transmission electron microscopy (STEM) and electron energy loss spectroscopy (EELS). The magnet-tipped cantilever was prepared for TEM analysis by attaching the leading edge of the cantilever to a copper TEM grid using a dual-beam FEI Strata 400 STEM FIB system. The TEM grid was loaded in the flipstage (tilted 90°) so that the magnet would be viewed top-down in the transmission electron microscope and so the cantilever could be rigidly mounted as shown in Figure 2.4. All STEM and EELS experiments were conducted using a 200 kV FEI Tecnai F20-ST STEM. A top-down, bright-field STEM image of the overhanging portion of the nickel nanomagnet is shown in Figure 2.5.² Strong grain boundary contrast indicates that the bulk of the nanomagnet was polycrystalline with a grain size of 20-40 nm, whereas the leading and side edges of the nanomagnet appeared amorphous.

EELS analysis was conducted to assay the elemental composition of the nanomagnets with nanometer resolution. In all spectra, the only observed elements were chromium, nickel, and oxygen. An example EELS spectrum is shown in Figure 2.6, with each of the peaks of interest labeled. The inset in Figure 2.6 shows a dark-field image of the leading edge of the nanomagnet; the small cross indicates the position of the electron beam during the EELS measurement.

EELS linescans were obtained to determine the composition of the nanomagnet. To compare the relative atomic concentrations of each element, scattering cross sections were obtained from DigitalMicrograph using the Hartree-Slater approximation [113]. The energy ranges over which the chromium, oxygen, and nickel peaks were integrated were 575 to 595 eV, 532.2 to 575.7 eV, and 855.5 to 955.5 eV, respectively. The convergence angle was 9 mrad and the collection angle was 20 mrad. The calculated scattering cross sections for chromium, oxygen, and nickel were 1245 barns, 880 barns, and 2006 barns, respectively.

²Figures 2.5 and 2.7 adapted with permission from S. A Hickman, E. W. Moore, S.-G. Lee, J. G. Longenecker, S. J. Wright, L. E. Harrell, and J. A. Marohn, ACS Nano **4**, 7141 (2010). Copyright 2010, American Chemical Society.

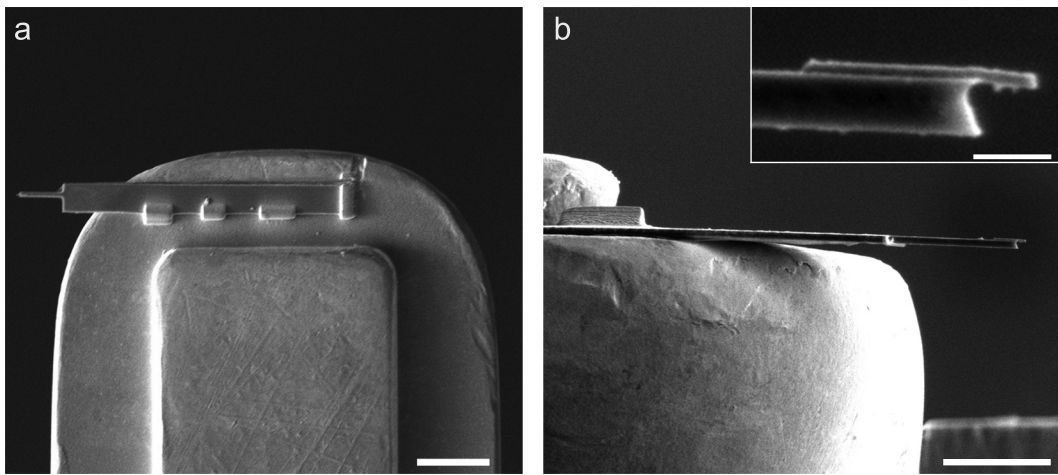


Figure 2.4: SEM images of the leading portion of a magnet-tipped cantilever attached to the center finger of a copper TEM grid. (a) Side-on view showing the cantilever mounted on the TEM grid. The TEM grid was mounted in the flipstage so that the cantilever could be positioned flush against the TEM grid finger and so that the magnet would be viewed top-down in the transmission electron microscope. Four rectangular patches of platinum were deposited to adhere the cantilever to the TEM grid. (b) View from the top of the TEM grid. A magnified side-on view of the magnet is shown in the inset. The scale bar in (a) represents 10 μm , the scale bar in (b) represents 5 μm , and the scale bar in the inset represents 500 nm.

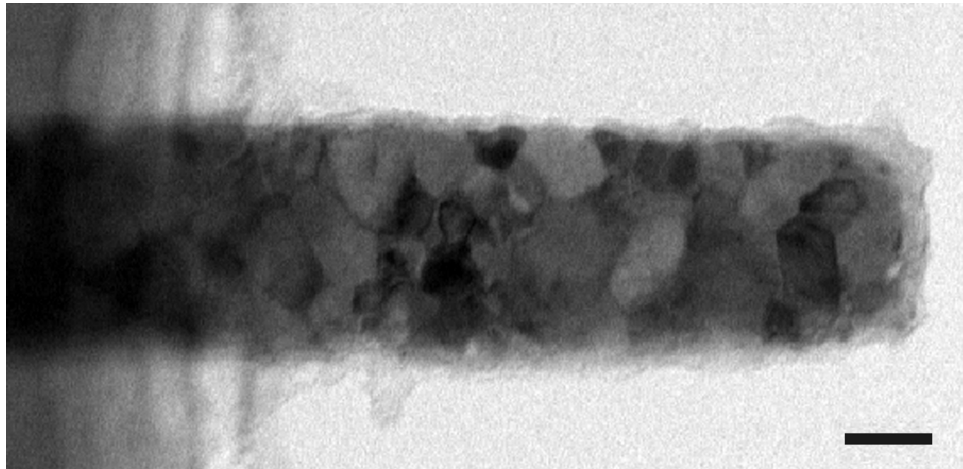


Figure 2.5: Bright-field STEM image of the overhanging portion of a 100 nm thick nickel nanomagnet with a 5 nm thick chromium adhesion layer underneath. The leading edge of the silicon cantilever is viewable on the left side of the image. The scale bar represents 50 nm.

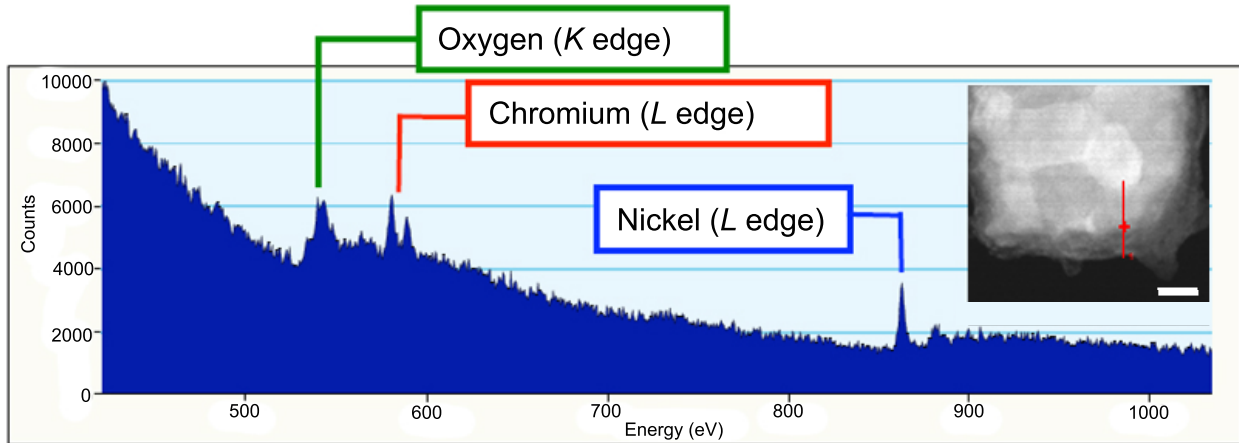


Figure 2.6: Example EELS spectrum showing the electron energy loss edges for oxygen, chromium, and nickel against the EELS background signal. The EELS measurement was one of many points taken along the red line shown in the dark-field STEM image of the magnet leading edge; the specific position of the electron beam during the measurement is indicated by the small red cross. The scale bar in the STEM image represents 20 nm.

EELS linescans were collected along the leading edge (Figure 2.7(a,b)) and side edge (Figure 2.7(c,d)) of the nickel nanomagnet. Near the center of the nanomagnet, the ratio of chromium to nickel was 0.05:1, which is in excellent agreement with the measured thicknesses for chromium and nickel of 5 nm and 100 nm, respectively. As both the leading and side edges were approached, the nickel concentration decreased and the oxygen concentration increased. In Figure 2.7(b), the concentration of nickel at the leading edge began to decrease 20 nm from the edge, implying that the leading 20 nm of magnetic material was damaged. In Figure 2.7(d), a 14 nm thick damage layer was observed. It should be noted that although the oxygen-to-nickel ratio of 1:1 for the damaged portion of the nanomagnet side edge could correspond to the formation of NiO, the anomalously high oxygen-to-nickel ratio at the leading edge cannot be explained solely by the formation of an oxide layer. It is likely that the additional oxygen content was due to oxygen-containing organic material on the magnet surface that was not measured in the EELS measurement.

In summary, SEM, STEM, and EELS analysis of four iterations of the Hickman protocol indicated that multiple factors contributed to nanomagnet damage during processing. As

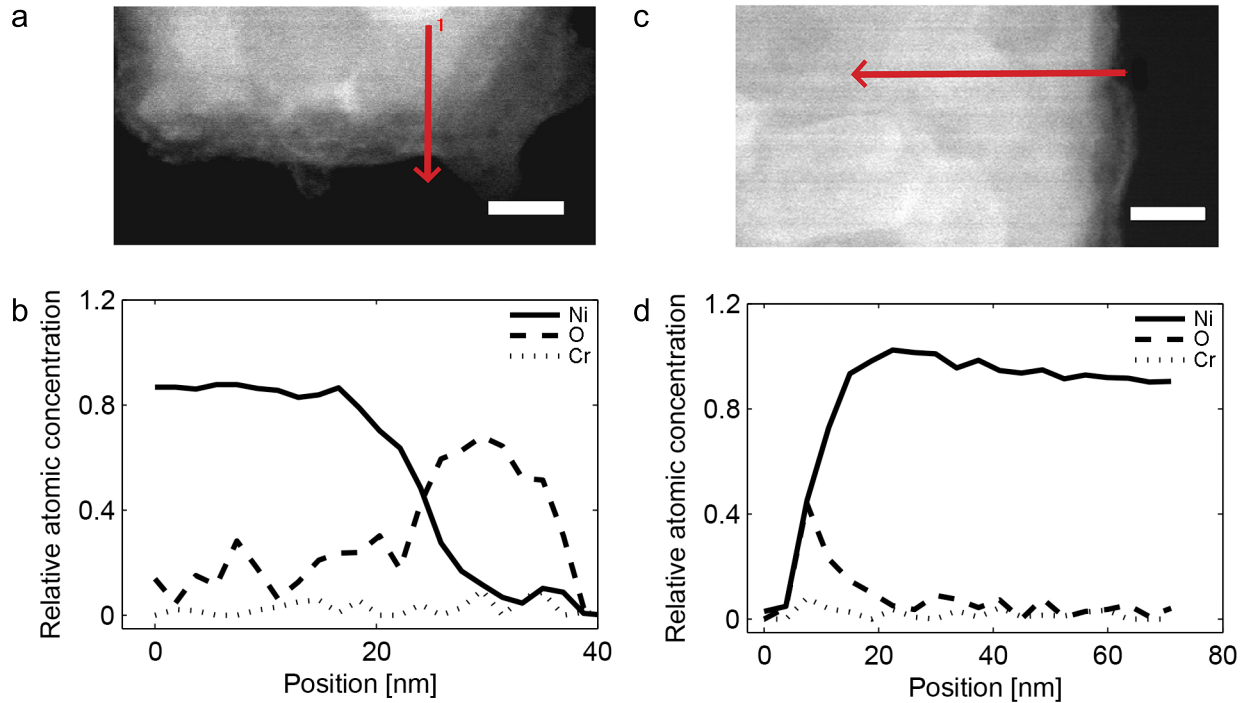


Figure 2.7: EELS linescans along the edges of the overhanging portion of a nickel nanomagnet. Dark-field STEM image (a) and relative EELS signal (b) for the leading edge of the nanomagnet are shown on the left-hand side. Dark-field STEM image (c) and relative EELS signal (d) for the side edge of the nanomagnet are shown on the right-hand side. The red arrows in the STEM images indicate the length and direction of the EELS linescans. The scale bars in (a) and (c) represent 20 nm. In the EELS scans, nickel, oxygen, and chromium are plotted using solid, dot-dashed, and dotted lines, respectively.

expected, silicide formation likely contributed to the damage mechanism. However, new findings indicated that damage also occurred during the PECVD SiO₂ processing step. When the nanomagnets were protected during the deposition of PECVD SiO₂, only 20 nm of damage was observed. These findings suggest that the use of barrier layers should be explored to make the Hickman protocol more robust against the formation of undesired nickel compounds, including nickel oxide and nickel silicide. The implementation of barrier layers in the Hickman protocol is discussed in the next section.

2.4 Barrier Layers Introduced to Prevent Nanomagnet Damage

The use of barrier layers to prevent silicidation of magnetic material was considered previously for the Hickman fabrication protocol, but only for cobalt magnetic material [91]. In Ref. 91, the use of a tantalum barrier layer was tested by evaporating 20 nm of tantalum under cobalt nanomagnets. To assess whether the barrier layer was effective, the magnets were coated with a thin layer of PECVD SiO₂ and annealed at 500°C for 5 min to mimic the heating conditions of the Bosch through-wafer silicon etch. The PECVD SiO₂ was then removed in BOE. The cobalt magnets appeared to be damaged after processing; however, it was inconclusive whether the damage was caused by the anneal or by other processing, since damage to cobalt nanomagnets was observed both for the annealed magnets and for control samples that were coated with PECVD SiO₂ but not annealed. In Ref. 91 the damage to the cobalt nanomagnets was attributed to the BOE etch that removed the PECVD SiO₂ after the anneal; data presented in Section 2.3 indicates that the damage instead may have occurred during the PECVD SiO₂ deposition.

The implementation of barrier layers to prevent damage to nickel magnetic material during the Hickman fabrication protocol had not been studied previously, nor had silicidation

or oxidation barriers been implemented in successful trials. The use of a magnet capping layer to prevent nickel oxidation and protect the magnets during the PECVD SiO₂ deposition step was of particular interest based on the findings of Section 2.3. Prevention of nickel silicide and nickel oxide have been demonstrated previously for other applications using tantalum and alumina (Al₂O₃) layers, respectively. Nickel silicide forms by the diffusion of nickel atoms into silicon above temperatures of 250°C [104, 105]. The introduction of a thin tantalum layer between a nickel film and a silicon substrate has been observed to inhibit the formation of nickel silicide until temperatures above 400°C [114]; 10 nm thick tantalum layers inhibited silicide growth of a Ni/Ta/Si sample for the full length of a 30 min anneal at 400°C, and a tantalum film that was just 2 nm thick prevented the formation of nickel silicide for the first 10 minutes of a 400°C anneal. Nickel oxidation occurs by the chemisorption of oxygen atoms onto the nickel surface. The oxidation of the nickel component of permalloy (Ni₈₁Fe₁₉) has been prevented by coating the permalloy surface with 1.5 nm of aluminum, which oxidized upon exposure to air to an alumina film that was less than 5 nm thick [115]. Conformal atomic layer deposition (ALD) alumina films have also been demonstrated to prevent oxidation; a sub-1 nm thick film (2 monolayers) deposited at 50°C successfully prevented the oxidation of silver film-over-nanosphere (AgFON) substrates, and remained stable for at least 9 months [116].

To determine whether tantalum and ALD alumina barrier layers would be effective at mitigating the formation of nickel silicide and nickel oxide during the integrated overhanging magnet-on-cantilever fabrication protocol of Ref. 81, a test sample was prepared and analyzed by EELS. The sample was deposited by e-beam evaporation of 100 nm of tantalum and 100 nm of nickel on a Si⟨100⟩ wafer, followed by ALD deposition of approximately 9 nm of alumina (processing temperature 110°C). The sample was annealed for 2 hours at 350°C, which was the highest temperature expected during processing steps of the Hickman fabrication protocol. The sample was cross-sectioned using a dual-beam FIB and assessed by STEM

and EELS using the parameters that were described in Section 2.3. In Figure 2.8, a bright-field STEM image of the cross-section of the film is shown on the left-hand side. The EELS linescan shown on the right-hand side of Figure 2.8 was collected along the transition from the nickel layer to the tantalum layer, as indicated by the arrow in the STEM image. The tantalum EELS signal was insufficient to quantify, but the relative concentrations of nickel and silicon were assessed. The primary finding was that no silicon was observed in the nickel or tantalum layers, indicating that the tantalum barrier layer had successfully prevented the formation of nickel silicide. Additional EELS linescans along the nickel-alumina interface (data not shown) indicated that oxygen was only contained in the top few nanometers of the nickel film. Oxidation of a few nanometers of nickel was expected since the unprotected nickel film was exposed to air prior to the deposition of the ALD alumina film. The absence of further oxidation indicated that using an ALD alumina film as a barrier against oxidation damage had been successful.

Based on the success of the barrier layer test sample, tantalum and ALD alumina barrier layers were incorporated into the Hickman fabrication protocol to assess their effectiveness at preventing the silicidation and oxidation of nickel nanomagnets, respectively. A schematic detailing the implementation of the barrier layers is shown in Figure 2.9. A tantalum layer that was 10 nm thick was deposited between the 5 nm thick chromium adhesion layer and the 100 nm thick nickel film using e-beam evaporation. Note that the thickness of the tantalum barrier layer was reduced from 100 nm for the test sample tantalum layer to only 10 nm for the nickel nanomagnets because nickel nanomagnet layers were observed to delaminate from 100 nm thick tantalum underlayers. A 7.5 nm thick ALD alumina film (processing temperature 110°C) was deposited after definition of the cantilevers and before deposition of the PECVD SiO₂ layer. Integration of ALD alumina into the fabrication protocol worked exceptionally well because alumina is etched readily in BOE. Thus, the ALD alumina was removed during the cantilever release of the magnet-on-cantilever fabrication protocol and

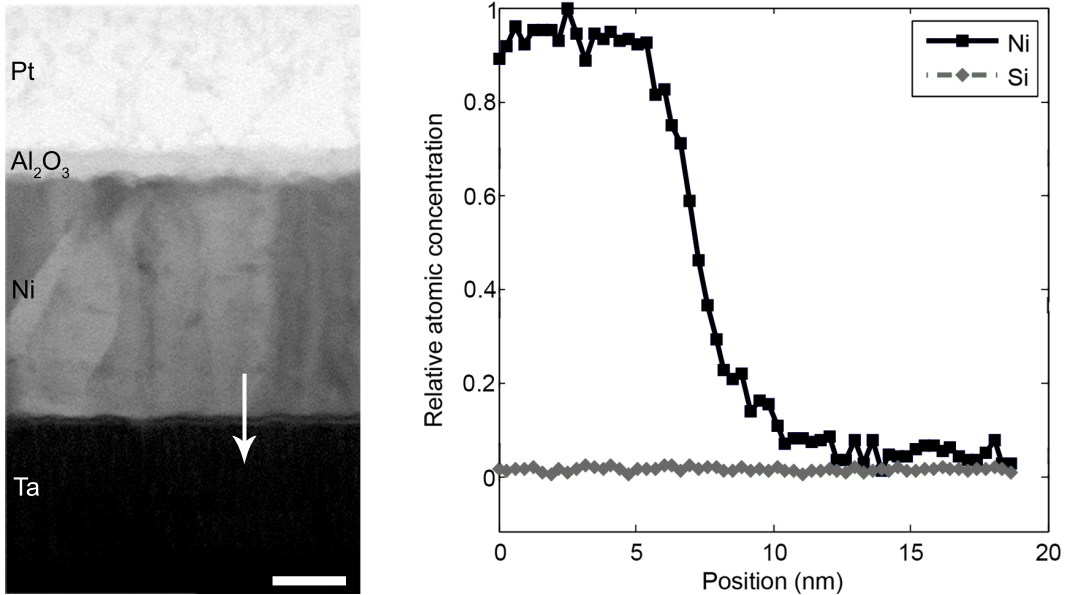


Figure 2.8: EELS analysis of a nickel film protected by tantalum and ALD alumina barrier layers to prevent the formation of nickel silicide and nickel oxide, respectively. The film was annealed at 350°C to mimic the conditions of the Bosch through-wafer silicon etch. A bright-field, cross-sectional STEM image is shown on the left-hand side. From top-to-bottom, the layers of the sample are a protective platinum coating deposited during the FIB sample preparation, ALD alumina (9 nm), nickel (100 nm), and tantalum (100 nm). The STEM scale bar represents 25 nm. The white arrow indicates the length and direction of the EELS linescan shown on the right-hand side of the image. The relative intensities of nickel (black squares) and silicon (gray diamonds) are shown. The EELS tantalum signal was too weak to measure.

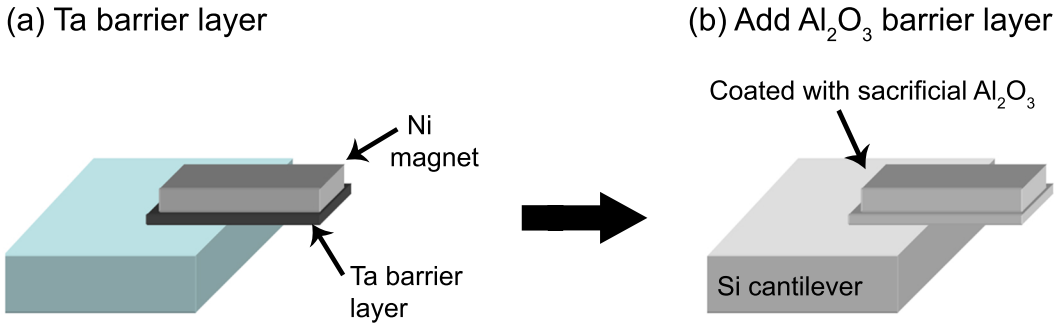


Figure 2.9: Schematic demonstrating how the tantalum and alumina barrier layers were incorporated into the revised overhanging magnet-tipped cantilever fabrication protocol. (a) The tantalum barrier layer was incorporated during the nickel nanomagnet evaporation. (b) After the front-side wafer processing was complete, the front side of the wafer was coated with conformal alumina before being coated with PECVD SiO_2 . The alumina film remained in place until the release of the cantilevers. The alumina was etched by BOE during the release, leaving the magnets and cantilevers free from an alumina coating after processing.

the nickel nanomagnets were free from added material at the completion of the process. The absence of material extending past the nanomagnet leading edge was critically important since the nanomagnet leading edge could be brought as close as 5 nm from the surface during MRFM experiments. It was also essential that the cantilever not be coated with any material after processing, since the cantilever resonance frequency and quality factor could be adversely affected.

SEM images of nickel nanomagnets fabricated with the tantalum and ALD alumina barrier layers are shown in Figure 2.10. The images show that the nickel nanomagnets remained visually intact after the cantilevers were released — a very promising finding when compared to the sub-1% yield of the original fabrication protocol. However, the true test of the success of the fabrication protocol was whether the nanomagnets remained well-magnetized after processing. The magnetization of one of the nickel nanomagnet-tipped cantilevers that had been processed with barrier layers was assessed by frequency-shift cantilever magnetometry (Figure 2.11). In cantilever magnetometry experiments [89, 93, 117], shifts in the cantilever frequency are measured as a function of applied magnetic field; in Figure 2.11, the field was

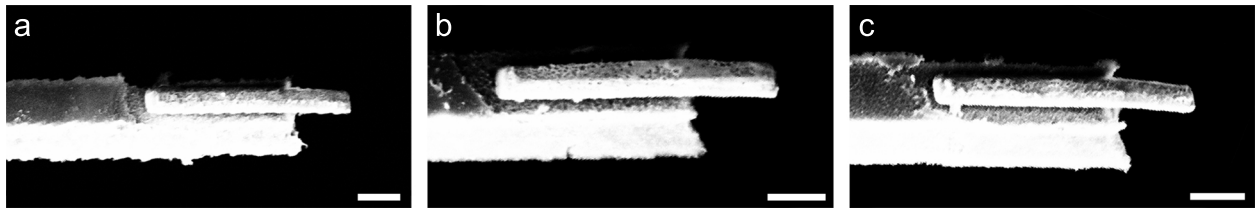


Figure 2.10: Side-view SEM images of released magnet-tipped cantilevers that were fabricated using tantalum and alumina barrier layers. The nanomagnets appeared to be visually intact. All scale bars represent 300 nm.

first swept from +5 T to -5 T, and then from -5 T to +5 T. Note that the divergence of the resonance frequency at positive fields in Figure 2.11 for the two directions of scanning was due to drift in the cantilever frequency during the ~ 2 hour measurement. A typical shift in frequency for a well-magnetized nickel nanomagnet of similar volume would be at least $\Delta f = 0.36$ Hz [81]. In Figure 2.11, the shift in resonance frequency was approximately 0.01 Hz. Thus, surprisingly and unfortunately, the nickel nanomagnet was almost completely demagnetized in spite of appearing visually intact.

The reason for the poorly-magnetized nickel nanomagnet has remained puzzling. The magnetic material was not expected to be pinned by the tantalum barrier layer, but even if pinning of the magnetic domain walls had occurred, we would not expect the associated anisotropy to be large enough to prevent full alignment of the tip's magnetization with the high external field of 5 T. Since cantilever magnetometry was only conducted on one magnet-tipped cantilever, it is possible that the majority of the nanomagnet delaminated during transport or loading into the instrument. Due to the two weeks of processing time required for each iteration of the integrated overhanging magnet-tipped cantilever fabrication protocol, with or without the incorporation of barrier layers, further trials to determine the reason for the discrepancy between the visually intact nanomagnets and the non-magnetic cantilever magnetometry findings were not pursued.

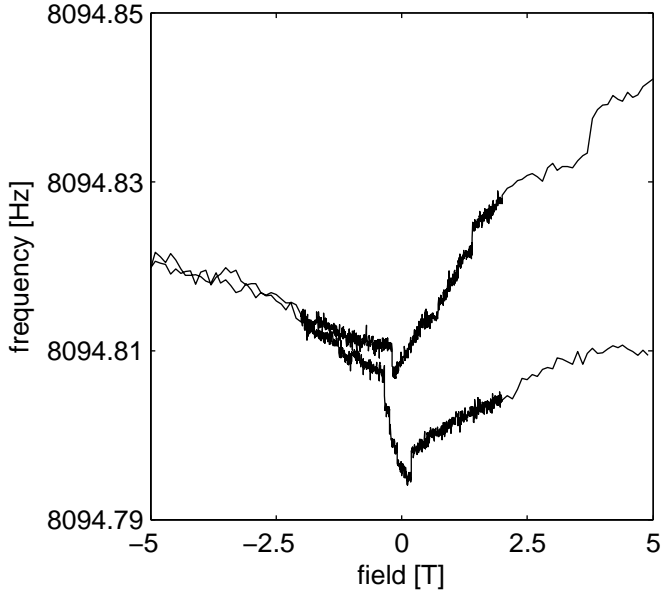


Figure 2.11: Frequency-shift cantilever magnetometry for a nickel nanomagnet fabricated using tantalum and alumina barrier layers. Data was collected by sweeping the applied magnetic field from +5 T to -5 T, and then from -5 T to +5 T. The divergence at positive fields for the two directions of scanning was due to thermal drift during the measurement.

2.5 Discussion

Out of the previously-developed techniques for the fabrication of attonewton-sensitivity cantilevers with integrated magnetic tips, the batch fabrication process introduced by Hickman *et al.* in Ref. 81 demonstrated the best promise for implementation in high resolution MRFM experiments. Yields were not reported by Hickman *et al.*, but damage to the nanomagnets was discussed at length [91]. For overhanging nickel magnets that did remain intact after the cantilevers were released, frequency-shift cantilever magnetometry indicated that the saturation magnetization $\mu_0 M_{\text{sat}}$ was only approximately 67% of the theoretical value of $\mu_0 M_{\text{sat}} = 0.6$ T. Attempts to switch to cobalt, which is a material with a factor of $3 \times$ larger saturation magnetization than nickel, were unsuccessful [91].

In this chapter, four attempts to reproduce the Hickman fabrication protocol for nickel nanomagnets were discussed. Three iterations of the process led to yields of less than 1%,

indicating that the process was either unreliable or contained processing steps that were incompatible with the stringent requirements for maintaining well-magnetized nickel magnetic material. During the fourth iteration of reproducing the Hickman protocol, a residual film did not lift off properly after the definition of the cantilevers. Surprisingly, the nanomagnets processed during this fourth iteration, most of which were still coated with the film after the cantilever release, remained visually intact underneath the residual film. EELS elemental analysis indicated that there was less than 20 nm of damage to the nickel leading edge of magnets that had been coated with a film during processing. These unexpected findings indicated that the use of barrier layers, and in particular a capping layer over the magnets to provide protection during PECVD SiO₂ deposition, could improve the yield of nanomagnet-tipped cantilevers.

The incorporation of barrier layers into the Hickman fabrication protocol were pursued in order to protect the magnets during PECVD SiO₂ deposition and to improve the robustness of the process against the formation of nickel silicide. When tantalum and ALD alumina barrier layers were added to the Hickman protocol, the overhanging magnets appeared to be visually intact after the release of the overhanging magnet-tipped cantilevers. However, frequency-shift cantilever magnetometry conducted on one of the magnets indicated that the nickel nanorods were nonmagnetic.

Even with the unexplained magnetometry data, it is clear that the implementation of barrier layers — and in particular the protection of the nanomagnets using ALD alumina — had a beneficial effect on the visual integrity of the nanomagnets. The results presented in this chapter thus indicate that the nanomagnets in the original Hickman fabrication protocol were damaged both by heating during the Bosch through-wafer etch and by interactions with the PECVD SiO₂ precursors. If the incorporation of barrier layers is considered further in future experiments, additional cantilever magnetometry and superconducting quantum

interference device (SQUID) measurements should be conducted to determine whether the cantilever magnetometry result in Figure 2.11 is correct.

If the nanomagnets are consistently demagnetized, then the use of other barrier layer materials could be considered, such as replacing the ALD alumina film with a metal film to encase the nanomagnets during the backside processing. However, a significant number of process integration challenges must be considered if the protective capping layer is changed. Nickel is damaged by BOE, so the capping layer must protect the nickel nanomagnets until 1-2 minutes before the end of the BOE cantilever release. However, if the film is still in place after the cantilever release, any stress in the capping layer film would instantly break the fragile cantilevers. Additionally, no barrier layer films could cover the cantilevers or extend more than 2-3 nm beyond the leading edge of the nanomagnets after the cantilevers are released, since the signal in MRFM experiments requires the close approach of the nanomagnets to the sample surface. Integration of alternative capping layers would likely require significant process development.

2.6 Moving Forward: A New Protocol is Needed to Improve Yield and Magnetization of Magnet-Tipped Cantilevers

With the 38 steps and 2 weeks of processing time required for each iteration of the Hickman protocol [81], conducting failure analysis was a slow and tedious process. The nanomagnets were deposited in one of the first processing steps, and all cantilever processing that followed the nanomagnet deposition had to be conducted within an acceptable heat budget and using compatible chemicals. The fabrication protocol also required that the nanomagnets be encased during multiple consecutive processing steps, which meant that they could not be imaged during the final half of the process. Thus, multiple factors contributing to the

damage mechanism were difficult to disentangle. Furthermore, if the magnetic material was switched to cobalt or to another material with a higher saturated magnetic moment than nickel, then new compatibility constraints would need to be considered and would again be difficult to assess.

These significant process integration challenges for the fabrication of integrated, overhanging magnet-on-cantilevers are precisely why many MRFM experiments are instead conducted using the sample-on-cantilever geometry [12, 48, 70, 71]. The highest-gradient magnetic particles employed in MRFM imaging experiments to date have all been fabricated off-cantilever [12, 48], where process integration is not required and the magnetic material can be analyzed immediately after deposition.

Chapters 3 through 5 of this thesis seek to answer the following question: Could the best of off-cantilever magnet fabrication methods be combined with the design of a high-gradient magnet-on-cantilever fabrication protocol? Continued progress towards the development of high-gradient magnetic tips on cantilevers — which requires higher magnet-on-cantilever yield, better-magnetized tips, and the use of new magnetic materials — would be greatly facilitated if there was a way to conduct rapid-prototyping fabrication trials with only a few days of processing time. Additionally, failure analysis could provide fast, conclusive results if the nanomagnets could be analyzed after each processing step. Unfortunately, both of these goals would be challenging, or impossible, to implement using the Hickman protocol.

Existing alternative techniques for the fabrication of magnets on cantilevers also do not meet the criteria for the rapid-prototyping development of cantilevers suitable for high-sensitivity magnet-on-cantilever MRFM experiments. FIB milling of magnetic material has been shown in MRFM experiments to not produce sufficiently high magnetic-field gradients [25, 53]. It is possible that FIB-induced damage could be minimized using low-energy ion beam polishing [118]; however, serial preparation and device-to-device variation would

still limit the desirability of FIB preparation. For magnet-tipped magnetic force microscopy (MFM) cantilevers, the magnetic material is oriented in the wrong direction [119]; a cone coated with magnetic material is oriented out of the plane of the cantilever instead of in-line with the cantilever, as required for high-sensitivity MRFM experiments. MFM tricks of adding magnetic coatings to narrow-diameter structures such as nanowires [120] or FIB-thinned silicon [121, 122], but with the tips oriented to extend inline past the cantilever leading edge, would (1) result in significant device-to-device variation and (2) have non-magnetic cores that would lower the total magnetic volume and the achievable MRFM signal strength. The electrodeposition of magnetic material on gold catalytic seeds at the ends of silicon nanowire cantilevers [123] would also lead to non-magnetic cores, as well as spherical magnetic particles with low tip-field gradients. The use of iron-filled multiwall carbon nanotubes (MWCNTs) [124] would result in 5 to 40 nm thick shells of carbon surrounding the magnetic material. Additionally, the 10-20 nm diameter magnetic material inside the MWCNTs could not be optimized for varying tip-sample separations (Eq. 1.9), and nanotubes have been found to be difficult to align precisely parallel to the cantilever length. And although directed assembly has been used in high yield to align silicon and rhodium nanowires [125], it is unclear how the necessary sacrificial electrodes could be incorporated into MRFM cantilever fabrication without incurring a different, but equally long, list of process integration challenges. One alternative batch-fabrication process that could be possible to implement would be to fabricate the cantilevers — including the backside processing — first [126], and to not pattern the nanomagnets until immediately before the cantilever release. However, the processing time required per trial would be equivalent whether the nanomagnets were fabricated before or after the definition of the cantilevers.

In Chapter 3, a novel approach is introduced to conduct rapid-prototyping fabrication trials of batch-fabricated nanomagnets that are attached to overhang attonewton-sensitivity cantilevers. In the protocol, batch-fabricated nanomagnets that overhang microscale, sus-

suspended silicon chips are prepared separately from attonewton-sensitivity cantilevers; the nanomagnets are then serially attached to the leading edge of cantilevers. This fabrication protocol indeed meets the goals discussed in this section: (1) the protocol is designed so that the magnets, which are fabricated off-cantilever, can be analyzed after any processing step using cantilever magnetometry or elemental characterization techniques such as EELS; (2) the fabrication of the magnets does not need to be compatible with the cantilever fabrication protocol; and (3) the magnet-tipped chip fabrication protocol requires only a few days of processing time, which makes it amenable to rapid prototyping experiments. By fabricating the magnets off-cantilever, process integration challenges are greatly minimized and can be adjusted for a variety of magnetic materials with different fabrication constraints, and by attaching the magnet-tipped chips to attonewton-sensitivity cantilevers, all of the benefits of working in the magnet-on-cantilever geometry can be retained. In Chapter 5 the benefit of using this combination batch-and-serial approach is confirmed by using a cobalt nanomagnet-tipped chip-on-cantilever assembly to detect NMR-MRFM signal. The tip-field gradient produced by the cobalt nanomagnet is as high as the gradient used in the 4-10 nm resolution imaging experiment of Degen *et al.* [12].

In future experiments it may be desirable to reintegrate the magnets and cantilevers into one batch-fabrication protocol. If so, cantilever processing steps could be added one-at-a-time to the magnet-tipped chips process of Chapter 3 to conclusively determine all steps contributing to the damage mechanism; since the nanomagnet chips are suspended, the chips could be lifted out after any processing step to conduct cantilever magnetometry or EELS experiments. The impact of adding barrier layers on the magnetization of the nanomagnets could also be reassessed using the rapid-prototyping technique.

Acknowledgements

Thanks to Steve Hickman for invaluable conversations regarding the proper implementation of the fabrication techniques used in Ref. 81. Thanks to Mick Thomas for assistance with TEM sample preparation, and to Pinshane Huang, John Grazul, and David Muller for assistance with STEM and EELS experiments. Coworker Eric Moore assisted with cantilever magnetometry, and undergraduate student Eric VanWerven assisted with integration of the tantalum barrier layer into the fabrication protocol. Work in this chapter was conducted with the financial support of the National Institutes of Health (Grant No. 5R01GM-070012), the Army Research Office MultiUniversity Research Initiative (Grant No. W911NF-05-1-0403), and the National Science Foundation through the Cornell Center for Nanoscale Systems (Grant Nos. EEC-0117770 and EEC-0646547). The transmission electron microscopy facility within the Cornell Center for Materials Research, which is supported by the National Science Foundation Materials Research Science and Engineering Centers program (Grant No. DMR-0520404), was used for TEM sample preparation, STEM imaging, and EELS analysis. Fabrication was conducted in the Cornell NanoScale Science and Technology Facility, a member of the National Nanotechnology Infrastructure Network, which is supported by the National Science Foundation (Grant No. ECS-0335765).